J. Fluid Mech. (2019), *vol.* 878, *pp.* 445–480. © Cambridge University Press 2019
doi:10.1017/jfm.2019.656

Wave power extraction from multiple oscillating water columns along a straight coast

Siming Zheng[1,†], Alessandro Antonini[2], Yongliang Zhang[3], Deborah Greaves[1], Jon Miles[1] and Gregorio Iglesias[4,1]

[1]School of Engineering, University of Plymouth, Drake Circus, Plymouth PL4 8AA, UK

[2]Department of Hydraulic Engineering, Delft University of Technology, 2628 CN Delft, The Netherlands

[3]State Key Laboratory of Hydroscience and Engineering, Tsinghua University, 100084 Beijing, China

[4]Centre for Marine Renewable Energy Ireland (MaREI), Environmental Research Institute and School of Engineering, University College Cork, Cork, P43 C573, Ireland

(Received 20 March 2019; revised 6 August 2019; accepted 6 August 2019;
first published online 13 September 2019)

The integration of oscillating water column (OWC) wave energy converters into a coastal structure (breakwater, jetty, pier, etc.) or, more generally, their installation along the coast is an effective way to increase the accessibility of wave power exploitation. In this paper, a theoretical model is developed based on the linear potential flow theory and eigenfunction matching method to evaluate the hydrodynamic performance of an array of OWCs installed along a vertical straight coast. The chamber of each OWC consists of a hollow vertical circular cylinder, which is half embedded in the wall. The OWC chambers in the theoretical model may have different sizes, i.e. different values of the radius, wall thickness and submergence. At the top of each chamber, a Wells turbine is installed to extract power. The effects of the Wells turbine together with the air compressibility are taken into account as a linear power take-off system. The hydrodynamic and wave power extraction performance of the multiple coast-integrated OWCs is compared with that of a single offshore/coast-integrated OWC and of multiple offshore OWCs. More specifically, we analyse the role of the incident wave direction, chamber size (i.e. radius, wall thickness and submergence), spacing between OWCs and number of OWCs by means of the present theoretical model. It is shown that wave power extraction from the coast-integrated OWCs for a certain range of wave conditions can be significantly enhanced due to both the constructive array effect and the constructive coast effect.

Key words: wave–structure interactions, surface gravity waves, wave scattering

1. Introduction

Many different concepts for wave energy conversion have been proposed (Clément *et al.* 2002; Drew, Plummer & Sahinkaya 2009; Rusu & Onea 2018). However, compared with other renewable energy technologies, such as solar, wind or tidal, wave power is rather immature, and relatively few wave energy converters (WECs)

† Email address for correspondence: siming.zheng@plymouth.ac.uk

https://doi.org/10.1017/jfm.2019.656 Published online by Cambridge University Press

have achieved fully commercial operation (Drew *et al.* 2009; Astariz & Iglesias 2015; Mustapa *et al.* 2017).

Among the various wave energy conversion concepts, the oscillating water column (OWC) is probably the most extensively investigated and best developed (Heath 2012; Falcão & Henriques 2016). An OWC is generally composed of a hollow chamber with its bottom open to the sea below the waterline. Subjected to ocean waves, the water column enclosed by the chamber moves up and down, applying pressure on the air within the chamber. The air is forced in and out of the chamber through a turbine installed at the top of the OWC, allowing for power extraction.

The cost of power is the major limitation to the uptake of WECs in commercial operation (Heath 2012; Di Lauro *et al.* 2019). This is a general issue with wave energy, not specific to OWC technology. A number of efforts have been made to achieve commercialization of OWCs (Viviano *et al.* 2016; Pawitan *et al.* 2019). The integration of OWCs into coastal structures, such as breakwaters, jetties and piers, or along sections of the coast, presents an effective way to increase significantly the attractiveness of wave power exploitation. The fact that the capture factor of WECs may be enhanced by their deployment along the coast (which may be referred to, for simplicity, as the coast effect) was reported for flap-type WECs by Sarkar, Renzi & Dias (2015) and Michele, Sammarco & d'Errico (2016), and also for oscillating buoys by Evans (1988), Zhao *et al.* (2018) and Zhang & Ning (2019). In this way, the economics of the OWC can be enhanced thanks to cost-sharing benefits, including construction, installation and maintenance (Boccotti 2007; Heras-Saizarbitoria, Zamanillo & Laskurain 2013; Arena *et al.* 2017; Mustapa *et al.* 2017). Reliability and survivability of the OWC can be improved as well, allowing power extraction during large wave conditions.

Many theoretical investigations have been devoted to wave power extraction by coast/breakwater-integrated OWCs. Evans & Porter (1995) proposed a two-dimensional (2-D) theoretical model to study the performance of an onshore OWC device that consists of a thin vertical surface-piercing lip in front of a vertical wall. It was illustrated that, by choosing proper submergence of the lip and the spacing distance between the lip and the wall, the incident wave power can be captured efficiently. The performance of a thin-walled OWC installed either at the tip of a thin fixed breakwater or along a straight coast was considered by Martins-Rivas & Mei (2009*a*,*b*), who developed theoretical models based on the linear potential flow theory to solve the three-dimensional (3-D) wave radiation/diffraction problems. To deal with the singular behaviours in the velocity field across the gap under the thin wall of OWC chamber, an integral equation for the horizontal velocity under the wall was employed in their models. The extracted power of the OWC at the tip of a thin breakwater was found to be reasonably insensitive to the incident wave direction, whereas the response of the OWC installed on a straight coast was strongly dependent on wave direction. The best performance occurred under normal incidence for most frequencies. Wave reflection at the coast means that the power captured by the OWC can be doubled. Lovas, Mei & Liu (2010) extended the theoretical model by Martins-Rivas & Mei (2009*a*,*b*) into a more general model that can be applied to more complex situations, i.e. a thin-walled OWC installed at a coastal corner. The captured power by the OWC at a concave corner was found to be significantly greater than that when the OWC was installed at the tip of a convex corner of right angle.

More recently, Zheng, Zhang & Iglesias (2019) developed a theoretical model of a coast/breakwater-integrated OWC, in which the effect of the thickness of the OWC chamber wall was considered. Subjected to a fixed outer radius, the thinner

https://doi.org/10.1017/jfm.2019.656 Published online by Cambridge University Press

the chamber wall, the larger and broader the main peaks of the frequency response of wave power capture width. Numerical and physical studies on a coast/breakwater-integrated OWC can be found in Morris-Thomas, Irvin & Thiagarajan (2007), He, Huang & Law (2012), Zhang, Zou & Greaves (2012), López & Iglesias (2014), Elhanafi *et al.* (2016), Falcão, Henriques & Gato (2016), López *et al.* (2016), He, Leng & Zhao (2017) and Howe & Nader (2017). However, most of these studies are focused on 2-D problems, and therefore miss fundamental dynamics related to direction changes in wave diffraction and radiation from complex-shaped structures.

In order to fully harness the available wave power in a region and to produce large quantities of energy for electrical grids, wave farms, i.e. arrays of OWCs, are likely to be deployed. For these OWCs deployed not far away from each other, cost-sharing benefits of installation and electrical power transmission can be made as well. On the basis of an analytical solution of hydrodynamic problems from an oscillating circular patch on the water surface, Nihous (2012) presented a model to predict wave power absorption from an array of OWCs. The OWC chamber was assumed to have a sufficiently shallow draught; thus diffraction effects were neglected in the model. A finite array of fixed OWCs without the restriction of shallow draught was considered by Nader *et al.* (2012) by applying a 3-D finite element method model. The complexity of hydrodynamic interactions between the OWCs within the array was highlighted. Later, a more realistic model with the air compressibility inside the OWC chamber taken into account was proposed (Sarmento & Falcão 1985; Nader, Zhu & Cooper 2014; López *et al.* 2020). The results showed that, for some certain wave frequencies, more power can be harnessed by the array of fixed OWCs compared with the total power that the same number of OWCs working in isolation could extract. Recently, Konispoliatis & Mavrakos (2016) developed an efficient theoretical model to investigate the performance of an array of free-floating OWCs. Major improvements in terms of extracted power were demonstrated for arrays with certain spacings between the OWCs. More recently, the hydrodynamic characteristics of a hybrid wave farm consisting of both OWCs and point-absorber WECs were investigated by Zheng, Zhang & Iglesias (2018).

Apart from the integration of OWCs into coastal structures and the deployment of OWCs in an array, various studies have also been carried out on the development of individual OWCs (López *et al.* 2014; Pereiras *et al.* 2015; Henriques *et al.* 2016; Elhanafi *et al.* 2017; Kurniawan *et al.* 2017; Ning, Zhou & Zhang 2018; Sheng & Lewis 2018; He *et al.* 2019).

To the authors' knowledge, most of the previous research work on OWCs has been focused on the investigation of either a single coast-integrated/offshore OWC or an array of offshore OWCs. In this article, the concept of integrating multiple OWCs into a straight coast is proposed. The chamber of each OWC mainly consists of a hollow vertical circular cylinder, which is cut away such that it is half open to the sea from a finite submergence to the seabed. To evaluate the hydrodynamic performance of these coast-integrated OWCs, a 3-D theoretical model is developed based on the linear potential flow theory and eigenfunction matching method. The water depth is assumed to be constant, in order to simplify the wave conditions. The effect of a Wells turbine installed at the top of each OWC together with the air compressibility are taken into account by means of a linear power take-off (PTO) system. Different from most of the previous reviewed 3-D theoretical models for a single coast-integrated thin-walled OWC, the present model can be used to study wave power extraction from multiple coast-integrated OWCs without the thin-wall restriction, i.e. the effect of the wall thickness of the OWC chamber is taken into consideration. The performance of the

https://doi.org/10.1017/jfm.2019.656 Published online by Cambridge University Press

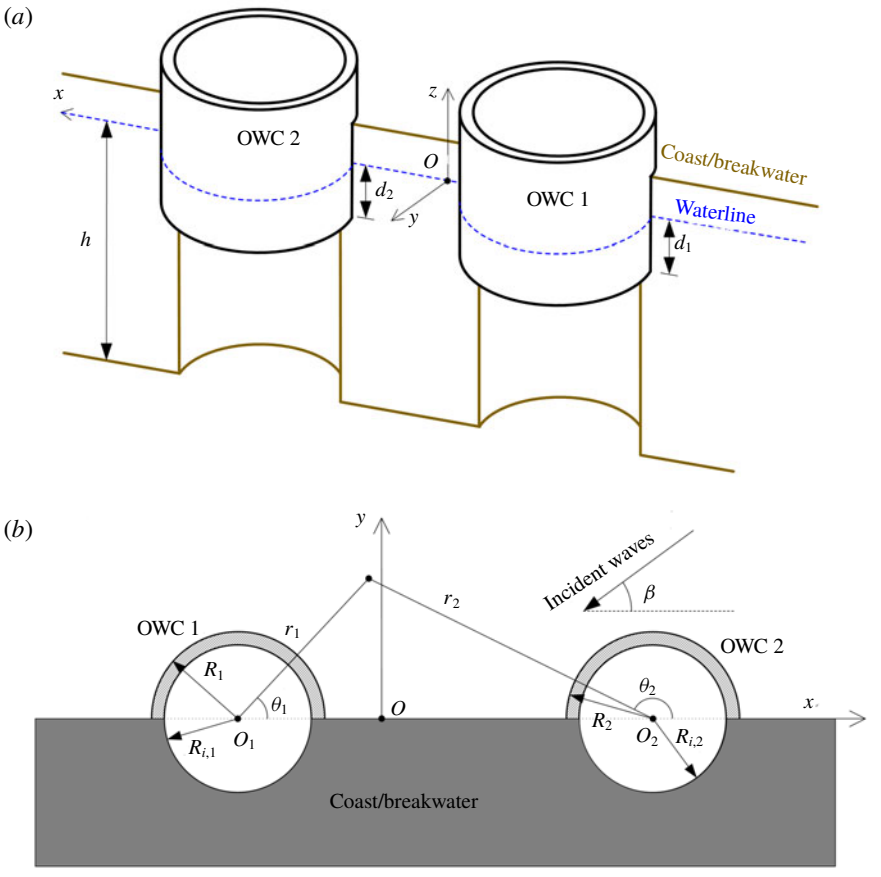


FIGURE 1. (Colour online) Definition sketch: (*a*) general layout of a pair of OWCs; (*b*) plan section with key dimensions.

multiple coast-integrated OWC system is compared with that of a single individual coast-integrated OWC, and also with that of single and multiple offshore OWCs, which consists of a stationary hollow vertical cylinder located in the open sea with the whole cylinder cut off at a finite distance from the seabed. The theoretical model is applied to explore the influences of incident wave direction, chamber size (i.e. radius, wall thickness and submergence), spacing distance between the OWCs and the number of OWCs on power extraction systematically.

2. Mathematical model

In the model, a number (N) of OWCs are conceptually installed along a straight coast in water of finite depth h (see figure 1, where $N = 2$ is taken as an example). A global Cartesian coordinate system $Oxyz$ is adopted with the Oxy plane at the mean water level and the Oxz plane at the sidewall of the coast. For the N vertical circular OWC chambers, the OWCs are numbered along the Ox axis in ascending order, and N local cylindrical coordinate systems, $O_n r_n \theta_n z_n$, are defined with their origins O_n at the central vertical axis of the nth OWC ($n = 1, 2, \ldots, N$). The O_n can be defined in Cartesian coordinate system $Oxyz$ as $(x_n, 0, 0)$. In addition, R_n, $R_{i,n}$ and d_n denote

https://doi.org/10.1017/jfm.2019.656 Published online by Cambridge University Press

the outer radius, inner radius and submergence of the nth OWC chamber, respectively; and D_n represents the distance between O_n and O_{n+1}.

For the coast-integrated OWCs subjected to regular incident waves with small wave steepness propagating in the direction of β relative to the coast (see figure 1), in the framework of linear potential flow theory, the fluid flow in the water domain is described by the velocity potential

$$\phi(x, y, z, t) = \mathrm{Re}[\Phi(x, y, z)\mathrm{e}^{-\mathrm{i}\omega t}]. \tag{2.1}$$

Here Φ is a complex spatial velocity potential independent of time, which needs to satisfy Laplace's equation in the fluid, in addition to certain linear boundary conditions, which will be given shortly; i is the imaginary unit; ω denotes the circular frequency of incident waves; and t is the time. The linear potential flow theory is not suitable for extreme waves, given that it does not account for either the viscous effect or the nonlinear wave dynamics.

Under linear theory, the spatial velocity potential Φ may be decomposed as the sum of scattering and radiation potentials, i.e.

$$\Phi = \Phi_0 + \sum_{n=1}^{N} p_n \Phi_n, \tag{2.2}$$

where Φ_0 is the scattering spatial velocity potential representing the wave field when the coast-integrated OWCs with the top of each chamber entirely open to the air (i.e. no dynamic air pressure) are subjected to the incident waves; p_n is the complex air pressure amplitude inside the nth OWC chamber; and Φ_n represents the spatial velocity potential due to a unit air pressure oscillation inside the nth OWC chamber while all the others are at rest.

Outside the OWCs, Φ_0 can be taken as the sum of two parts, $\Phi_0 = \Phi_I + \Phi_D$, where Φ_I is the spatial velocity potential representing the wave field due to the incident waves in the absence of OWCs, which includes both the incident plane wave and a plane wave reflected by the wall, and Φ_D is the diffracted spatial velocity potential due to the presence of the OWCs. In the nth local cylindrical coordinate system $O_n r_n \theta_n z$, Φ_I can be written as (Zheng & Zhang 2015)

$$\Phi_I(r_n, \theta_n, z) = -\frac{2\mathrm{i}gA}{\omega}\frac{Z_0(z)}{Z_0(0)}\mathrm{e}^{-\mathrm{i}k_0 x_n \cos\beta}\sum_{m=0}^{\infty}\varepsilon_m(-\mathrm{i})^m \mathrm{J}_m(k_0 r_n)\cos(m\beta)\cos(m\theta_n). \tag{2.3}$$

Here A is the amplitude of incident waves; g denotes the gravitational acceleration; $\varepsilon_m = 1$ for $m = 0$, whereas $\varepsilon_m = 2$ for $m > 0$; k_0 is the wavenumber, which satisfies the dispersion relation $\omega^2 = gk_0 \tanh(k_0 h)$; J_m denotes the Bessel function of order m; and $Z_0(z)$ is an eigenfunction given by

$$Z_0(z) = N_0^{-1/2}\cosh[k_0(z + h)], \quad N_0 = \frac{1}{2}\left[1 + \frac{\sinh(2k_0 h)}{2k_0 h}\right]. \tag{2.4a,b}$$

The governing equation in the water domain, the free-surface boundary conditions, and the body boundary conditions that Φ_χ ($\chi = 0, 1, 2, \ldots, N$) should satisfy are given as follows:

$$\nabla^2 \Phi_\chi = 0, \quad \text{in water}, \tag{2.5}$$

https://doi.org/10.1017/jfm.2019.656 Published online by Cambridge University Press

$$\frac{\partial \Phi_\chi}{\partial n} = 0, \quad \text{on all solid boundaries,} \tag{2.6}$$

$$\left(\frac{\partial \Phi_\chi}{\partial z} - \frac{\omega^2}{g}\Phi_\chi\right)\Big|_{z=0} = \delta_{\chi,n}\frac{\mathrm{i}\omega}{\rho g},$$
on the water surface inside the nth OWC chamber, (2.7)

$$\left(\frac{\partial \Phi_\chi}{\partial z} - \frac{\omega^2}{g}\Phi_\chi\right)\Big|_{z=0} = 0,$$
on the water surface outside the nth OWC chamber, (2.8)

in which $\delta_{\chi,n}$ is the Kronecker delta function, which is equal to 1 when $\chi = n$, and is equal to 0 otherwise; and ρ represents the water density.

Additionally, it is required that Φ_D and Φ_χ ($\chi = 1, 2, \ldots, N$) are outgoing for $r_n \to \infty$.

3. Solution of scattering and radiated potentials

3.1. *Scattering and radiated spatial potentials in different regions*

The general solution of the potential Φ_χ in the region enclosed by the nth OWC, i.e. $r_n \in [0, R_{i,n}]$, $\theta_n \in [0, 2\pi]$, $z \in [-h, 0]$, is formally expressed as

$$\Phi^{in}_{\chi,n}(r_n, \theta_n, z) = \sum_{m=-\infty}^{\infty}\sum_{l=0}^{\infty}\frac{\tilde{\mathrm{I}}_m(k_l r_n)}{k_l \tilde{\mathrm{I}}'_m(k_l R_{i,n})}A^{\chi,n}_{m,l}Z_l(z)\mathrm{e}^{\mathrm{i}m\theta_n} - \mathrm{i}\frac{\delta_{\chi,n}}{\rho\omega}. \tag{3.1}$$

Here $A^{\chi,n}_{m,l}$ are the unknown coefficients to be solved;

$$\tilde{\mathrm{I}}_m(k_l r_n) = \begin{cases} \mathrm{J}_m(k_l r_n), & l = 0, \\ \mathrm{I}_m(k_l r_n), & l = 1, 2, 3, \ldots, \end{cases} \tag{3.2}$$

in which I_m denotes the modified Bessel function of the first kind of order m; k_l is the eigenvalue, which is given by (e.g. Falnes 2002)

$$\omega^2 = -gk_l \tan(k_l h), \quad l = 1, 2, 3, \ldots; \tag{3.3}$$

and the corresponding eigenfunction $Z_l(z)$ is defined by

$$Z_l(z) = N_l^{-1/2}\cos[k_l(z+h)], \quad N_l = \frac{1}{2}\left[1 + \frac{\sin(2k_l h)}{2k_l h}\right], \quad l = 1, 2, 3, \ldots. \tag{3.4a,b}$$

The eigenfunctions $Z_0(z)$ and $Z_l(z)$, as given in (2.4) and (3.4), form a complete orthogonal set in $z \in [-h, 0]$:

$$\int_{-h}^{0} Z_m(z)Z_l(z)\,\mathrm{d}z = h\delta_{m,l}, \quad m, l = 0, 1, 2, 3, \ldots. \tag{3.5}$$

In the region beneath the nth OWC chamber wall, i.e. $r_n \in [R_{i,n}, R_n]$, $\theta_n \in [0, \pi]$, $z \in [-h, -d_n]$, the potential Φ_χ can be expressed as

https://doi.org/10.1017/jfm.2019.656 Published online by Cambridge University Press

$$\Phi_{\chi,n}^{ring}(r_n,\theta_n,z) = \sum_{m=0}^{\infty}\left[F_{m,0}^{\chi,n}(r_n)+\sum_{l=1}^{\infty}\left(C_{m,l}^{\chi,n}\frac{\mathrm{I}_m(\beta_{n,l}r_n)}{\mathrm{I}_m(\beta_{n,l}R_n)} + D_{m,l}^{\chi,n}\frac{\mathrm{K}_m(\beta_{n,l}r_n)}{\mathrm{K}_m(\beta_{n,l}R_n)}\right)\cos[\beta_{n,l}(z+h)]\right]\cos(m\theta_n), \tag{3.6}$$

which satisfies the no-flux boundary condition on the coast ($\theta_n = 0$ and π). Therein,

$$F_{m,0}^{\chi,n}(r_n) = \begin{cases} C_{m,0}^{\chi,n} + D_{m,0}^{\chi,n}\left[1+\ln\left(\dfrac{r_n}{R_n}\right)\right], & m=0, \\ C_{m,0}^{\chi,n}\left(\dfrac{r_n}{R_n}\right)^{|m|} + D_{m,0}^{\chi,n}\left(\dfrac{r_n}{R_n}\right)^{-|m|}, & m\neq 0, \end{cases} \tag{3.7}$$

in which $C_{m,l}^{\chi,n}$ and $D_{m,l}^{\chi,n}$ are the unknown coefficients to be determined; K_m is the modified Bessel function of the second kind of order m; and $\beta_{n,l}$ is the lth eigenvalue given by

$$\beta_{n,l} = \frac{l\pi}{h-d_n}, \quad l = 0, 1, 2, 3, \ldots. \tag{3.8}$$

In the region outside the OWC chambers and in front of the coast extending towards infinite distance horizontally, i.e. $r_n \in [R_n, \infty]$, $\theta_n \in [0, \pi]$, $z \in [-h, 0]$, the potential Φ_χ can be expressed as

$$\Phi_{\chi}^{out}(r_n,\theta_n,z) = \delta_{\chi,0}\Phi_I + \sum_{j=1}^{N}\Phi_{\chi,j}^{out}, \tag{3.9}$$

where $\Phi_{\chi,j}^{out}$ represents the velocity potential component diffracted/radiated from the jth OWC, and it can be written in the jth local cylindrical coordinate $O_j r_j \theta_j z$ as

$$\Phi_{\chi,j}^{out}(r_j,\theta_j,z) = \sum_{m=0}^{\infty}\sum_{l=0}^{\infty}E_{m,l}^{\chi,j}\frac{\tilde{\mathrm{K}}_m(k_l r_j)}{\tilde{\mathrm{K}}_m(k_l R_j)}\cos(m\theta_j)Z_l(z), \tag{3.10}$$

which satisfies the no-flux boundary condition on the coast ($\theta_j = 0$ and π). Here $E_{m,l}^{\chi,j}$ are the unknown coefficients to be determined; and

$$\tilde{\mathrm{K}}_m(k_l r_j) = \begin{cases} \mathrm{H}_m(k_l r_j), & l=0, \\ \mathrm{K}_m(k_l r_j), & l=1,2,3,\ldots, \end{cases} \tag{3.11}$$

where H_m denotes the Hankel function of the first kind of order m.

Following Graf's addition theorem for Bessel functions (Abramowitz & Stegun 1964),

$$\tilde{\mathrm{K}}_m(k_l r_j)\cos(m\theta_j) = \sum_{m'=-\infty}^{\infty}\tilde{\mathrm{K}}_{m+m'}(k_l R_{jn})\tilde{\mathrm{I}}_{m'}(k_l r_n)\mathrm{e}^{\mathrm{i}(m\alpha_{jn}+m'\alpha_{nj})}\cos(m'\theta_n), \quad r_n \leqslant R_{jn}, \tag{3.12}$$

where R_{jn} and α_{jn} denote the norm and the angle of vector $\overrightarrow{O_jO_n}$, respectively. Therefore, the expression of $\Phi_{\chi,j}^{out}$ can be transformed from the jth local cylindrical

https://doi.org/10.1017/jfm.2019.656 Published online by Cambridge University Press

coordinate into the nth one, and (3.9) is ultimately expressed in the local cylindrical coordinate $O_n r_n \theta_n z$ by

$$\Phi_\chi^{out}(r_n, \theta_n, z) = \delta_{\chi,0}\Phi_I + \sum_{m=0}^{\infty}\sum_{l=0}^{\infty} E_{m,l}^{\chi,n}\frac{\tilde{\mathrm{K}}_m(k_l r_n)}{\tilde{\mathrm{K}}_m(k_l R_n)}\cos(m\theta_n)Z_l(z)$$
$$+ \sum_{\substack{j=1,\\ j\neq n}}^{N}\sum_{m=0}^{\infty}\sum_{l=0}^{\infty}\frac{E_{m,l}^{\chi,j}Z_l(z)}{\tilde{\mathrm{K}}_m(k_l R_j)}\sum_{m'=-\infty}^{\infty}\tilde{\mathrm{K}}_{m+m'}(k_l R_{jn})\tilde{\mathrm{I}}_{m'}(k_l r_n)\mathrm{e}^{\mathrm{i}(m\alpha_{jn}+m'\alpha_{nj})}\cos(m'\theta_n),$$
$$\text{for } r_n \leqslant R_{jn}. \tag{3.13}$$

3.2. *Method of computation for unknown coefficients*

It is easy to check that the governing equation and all the boundary conditions given in (2.5)–(2.8), except the no-flux condition on the inner and outer cylindrical surfaces of each OWC chamber $r_n = R_n$ and $r_n = R_{i,n}$, have been satisfied by the scattering and radiated spatial potentials in different regions, as expressed in § 3.1, regardless of the values of the unknown coefficients. Note that the no-flux condition at $r_n = R_n$ and $r_n = R_{i,n}$, together with the pressure and velocity continuity conditions on the interfaces of each two adjacent regions, should be satisfied as well, which can be applied to solve the unknown coefficients.

The continuity conditions for the scattering and radiated spatial potentials are given as follows:

(1) Continuity of normal velocity at the boundary $r_n = R_{i,n}$:

$$\left.\frac{\partial \Phi_{\chi,n}^{in}}{\partial r_n}\right|_{r_n=R_{i,n}} = \begin{cases} 0, & z\in[-d_n, 0],\ \theta_n\in[0,\pi], \\ & \text{and } z\in[-h, 0],\ \theta_n\in[\pi, 2\pi], \\ \left.\dfrac{\partial \Phi_{\chi,n}^{ring}}{\partial r_n}\right|_{r_n=R_{i,n}}, & z\in[-h, -d_n],\ \theta_n\in[0,\pi]. \end{cases} \tag{3.14}$$

(2) Continuity of normal velocity at the boundary $r_n = R_n$:

$$\left.\frac{\partial \Phi_{\chi,n}^{out}}{\partial r_n}\right|_{r_n=R_n} = \begin{cases} 0, & z\in[-d_n, 0],\ \theta_n\in[0,\pi], \\ \left.\dfrac{\partial \Phi_{\chi,n}^{ring}}{\partial r_n}\right|_{r_n=R_n}, & z\in[-h, -d_n],\ \theta_n\in[0,\pi]. \end{cases} \tag{3.15}$$

(3) Continuity of pressure at the boundary $r_n = R_{i,n}$:

$$\Phi_{\chi,n}^{ring}|_{r_n=R_{i,n}} = \Phi_{\chi,n}^{in}|_{r_n=R_{i,n}}, \quad z\in[-h, -d_n],\ \theta_n\in[0,\pi]. \tag{3.16}$$

(4) Continuity of pressure at the boundary $r_n = R_n$:

$$\Phi_{\chi,n}^{out}|_{r_n=R_n} = \Phi_{\chi,n}^{ring}|_{r_n=R_n}, \quad z\in[-h, -d_n],\ \theta_n\in[0,\pi]. \tag{3.17}$$

Inserting the expressions of $\Phi_{\chi,n}^{in}$, $\Phi_{\chi,n}^{ring}$ and Φ_χ^{out} as given in § 3.1 into the above continuity conditions, i.e. (3.14)–(3.17), and making use of the orthogonality of both trigonometric functions and eigenfunctions, the unknown coefficients $A_{m,l}^{\chi,n}$, $C_{m,l}^{\chi,n}$ and $D_{m,l}^{\chi,n}$ can be determined by solving a linear algebraic system after truncation (Zheng & Zhang 2015, 2016; Yu *et al.* 2019). For convenience, the details of the derivations can be found in appendix A.

https://doi.org/10.1017/jfm.2019.656 Published online by Cambridge University Press

3.3. *Wave excitation volume flux and hydrodynamic coefficients*

The upward displacement of the water surface inside the nth OWC chamber, i.e. the wave excitation volume flux of the nth OWC, induced by scattering waves can be written as

$$\begin{aligned} Q_e^{(n)} &= \int_0^{2\pi}\int_0^{R_{i,n}} \left.\frac{\partial \Phi_{0,n}^{in}(r_n,\theta_n,z)}{\partial z}\right|_{z=0} r_n\,\mathrm{d}r_n\,\mathrm{d}\theta_n \\ &= \frac{2\pi\omega^2 R_{i,n}}{g}\left(-\frac{A_{0,0}^{0,n}}{k_0^2}Z_0(0)+\sum_{l=1}^{\infty}\frac{A_{0,l}^{0,n}}{k_l^2}Z_l(0)\right). \end{aligned} \tag{3.18}$$

In a similar way, the volume flux of the nth OWC due to the radiated velocity potential induced by the unit air pressure oscillation inside the χth OWC chamber can be evaluated by

$$Q_\chi^{(n)} = \frac{2\pi\omega^2 R_{i,n}}{g}\left(-\frac{A_{0,0}^{\chi,n}}{k_0^2}Z_0(0)+\sum_{l=1}^{\infty}\frac{A_{0,l}^{\chi,n}}{k_l^2}Z_l(0)\right) = -(c_\chi^{(n)} - \mathrm{i}a_\chi^{(n)}), \tag{3.19}$$

in which $c_\chi^{(n)}$ and $a_\chi^{(n)}$ on the right of the second equals sign are the hydrodynamic coefficients, more specifically, the so-called radiation damping and added mass, respectively.

The method as shown in (3.19) is a straightforward way to calculate the hydrodynamic coefficient, and is referred to here as the direct method. It is worth noting that there is an alternative approach based on the Haskind relation, which can be employed to evaluate $c_\chi^{(n)}$ indirectly (e.g. Falnes 2002; Martins-Rivas & Mei 2009*a*),

$$c_\chi^{(n)} = \frac{k}{8\pi\rho g c_g A^2}\int_0^{\pi} Q_e^{(n)}(\beta)Q_e^{(\chi)*}(\beta)\,\mathrm{d}\beta, \tag{3.20}$$

where the superscript $*$ denotes complex conjugate, c_g denotes the wave group velocity and k is used to represent k_0 for the sake of simplicity. The Haskind-type identity as given in (3.20) links the radiation and scattering problems and presents a way to check the accuracy of the proposed theoretical model.

4. Relation between power take-off system and hydrodynamic problems

4.1. *Response of the OWCs*

The wave scattering and radiation problems are coupled by the PTO system. Assuming the mass flux through the Wells turbines is proportional to the chamber air pressure and the effect of air compressibility in the chamber is linear, following Sarmento & Falcão (1985) and Martins-Rivas & Mei (2009*a*,*b*), the complex air pressure amplitude in each OWC chamber is related to the scattering and radiated velocity potentials, resulting in the following matrix equation:

$$[-\mathrm{i}(\boldsymbol{M}_{PTO}+\boldsymbol{M})+(\boldsymbol{C}_{PTO}+\boldsymbol{C})]\boldsymbol{p} = \boldsymbol{Q}_e. \tag{4.1}$$

Here $\boldsymbol{M}_{PTO}$ is a diagonal matrix of size $N\times N$, adapted to consider the effect of air compressibility, and the nth element in the diagonal of $\boldsymbol{M}_{PTO}$ can be expressed as $\omega V_n/(v^2\rho_0)$, in which V_n is the air chamber volume of the nth OWC, v denotes the sound velocity in air and ρ_0 represents the static air density; $\boldsymbol{C}_{PTO}$ is a diagonal

https://doi.org/10.1017/jfm.2019.656 Published online by Cambridge University Press

matrix of size $N \times N$ as well, and it is used to represent the damping of the PTO system of each OWC, which depends on the rotational speed of the turbines, their specification and design, and also the static air density; $\boldsymbol{M}$ and $\boldsymbol{C}$ are two matrices of size $N \times N$ that represent the hydrodynamic coefficients that correspond to $a_\chi^{(n)}$ and $c_\chi^{(n)}$, respectively; and $\boldsymbol{p}$ is a column vector of length N that includes all the air pressure responses of the multiple OWCs p_n, $n = 1, 2, \ldots, N$. The forcing term $\boldsymbol{Q}_e$ is a column vector of length N including the complex wave excitation volume flux acting on each OWC $Q_e^{(n)}$, $n = 1, 2, \ldots, N$.

As $\boldsymbol{M}$, $\boldsymbol{C}$ and $\boldsymbol{Q}_e$ have already been theoretically evaluated in the previous sections, and $\boldsymbol{M}_{PTO}$ and $\boldsymbol{C}_{PTO}$ are known for a specified PTO system, the response of the OWCs can be easily determined by solving the Nth-order complex matrix equation (4.1).

4.2. *Wave power extraction*

Once the air pressure response in each OWC is obtained, the time-averaged power output by these coast-integrated OWCs can be directly calculated by (e.g. Falnes 2002)

$$P = \tfrac{1}{2}\boldsymbol{p}^\dagger \boldsymbol{C}_{PTO}\boldsymbol{p} = \tfrac{1}{2}\|\boldsymbol{C}_{PTO}^{1/2}\boldsymbol{p}\|^2, \tag{4.2}$$

where the superscript † denotes complex-conjugate transpose. Since $\boldsymbol{C}_{PTO}$ is a real diagonal matrix, the second equality holds, in which $\|\cdot\|$ represents the two-norm of a vector.

Following Lovas *et al.* (2010), the dimensionless coefficients of $Q_e^{(n)}$, the hydrodynamic coefficients $c_\chi^{(n)}$ and $a_\chi^{(n)}$, and the corresponding PTO parameters can be defined as follows:

$$\bar{Q}_e^{(n)} = \frac{\sqrt{g/h}}{Ahg}Q_e^{(n)}, \quad (\bar{c}_\chi^{(n)}, \bar{a}_\chi^{(n)}, \bar{c}_{PTO}^{(n)}, \bar{a}_{PTO}^{(n)}) = \frac{\rho\sqrt{g/h}}{h}(c_\chi^{(n)}, a_\chi^{(n)}, c_{PTO}^{(n)}, a_{PTO}^{(n)}), \tag{4.3a,b}$$

with which the time-averaged power absorption as given in (4.2) can be rewritten in terms of the wave capture factor:

$$\eta = \frac{2kP}{\rho g A^2 c_g} = \frac{khg}{c_g\sqrt{g/h}}\|\bar{\boldsymbol{C}}_{PTO}^{1/2}[-\mathrm{i}(\bar{\boldsymbol{M}}_{PTO} + \bar{\boldsymbol{M}}) + (\bar{\boldsymbol{C}}_{PTO} + \bar{\boldsymbol{C}})]^{-1}\bar{\boldsymbol{Q}}_e\|^2, \tag{4.4}$$

where the overbar indicates that the corresponding matrix is written in non-dimensional format.

The rest of this paper focuses on the particular case in which all the OWCs have the same size and the spacing between adjacent OWCs is constant, unless otherwise specified. Moreover, all the OWCs are assumed to employ the same PTO system. Hence, for the sake of convenience, $R_n = R$, $R_{i,n} = R_i$, $d_n = d$, $D_n = D$, $c_{PTO,n} = c_{PTO}$ and $a_{PTO,n} = a_{PTO}$ are adopted, with which (4.4) simplifies to

$$\eta = \frac{khg\bar{c}_{PTO}}{c_g\sqrt{g/h}}\|[-\mathrm{i}(\bar{a}_{PTO}\boldsymbol{I} + \bar{\boldsymbol{M}}) + (\bar{c}_{PTO}\boldsymbol{I} + \bar{\boldsymbol{C}})]^{-1}\bar{\boldsymbol{Q}}_e\|^2, \tag{4.5}$$

where $\boldsymbol{I}$ represents the square identity matrix of size $N \times N$. The chamber size and chamber geometry of each OWC are fixed and cannot be easily adjusted. Following Lovas *et al.* (2010) and Martins-Rivas & Mei (2009*a*,*b*), here the value of a_{PTO} is calculated based on $\rho/\rho_0 = 1000$, $v = 340$ m s^{-1}, $h = 10$ m and $V_0 = \pi R^2 h$, as $a_{PTO} = \omega V_0/(v^2\rho_0)$. As a comparison, it might be more feasible to vary the value of c_{PTO},

https://doi.org/10.1017/jfm.2019.656 Published online by Cambridge University Press

e.g. to use several turbines and control the blade angle and rotation speed, to strive for high efficiency for a wide range of wave frequencies. In this paper, the corresponding optimal PTO damping is considered equal to the optimum coefficient of the same coast-integrated OWC when working in isolation (Lovas *et al.* 2010; Martins-Rivas & Mei 2009*a*,*b*). The wave power capture factor contributed by the nth OWC is denoted by η_n.

Apart from the wave power capture factor η, a q-factor is adopted as well to evaluate the effect of the hydrodynamic interaction between the OWCs on power extraction:

$$q = \frac{\eta}{N\eta_0}, \tag{4.6}$$

where η_0 represents the maximum wave capture factor of an isolated coast-integrated OWC. If $q > 1$, using an array of OWCs along the coast plays a constructive role in power absorption. Whereas if $q < 1$, a destructive effect is induced by the hydrodynamic interaction between the multiple coast-integrated OWCs.

In a similar way, the influence of the coast, i.e. the reflection effect, may be evaluated by

$$q_c = \frac{\eta}{\eta'}, \tag{4.7}$$

in which η' denotes the wave capture factor of the corresponding offshore OWCs.

As given in (4.6) and (4.7), the subscript 0 and the superscript prime represent the individual single isolated situation and the offshore situation, respectively. Hence, $q' = \eta'/(N\eta_0')$ can be used as the array factor to denote the constructive or destructive hydrodynamic interaction between an array of offshore OWCs on power extraction, in which η_0' is the power capture factor of a single offshore OWC. Similarly, $q_{c,0} = \eta_0/\eta_0'$ can be used to calculate the reflection effect of the coast on a single coast-integrated OWC.

5. Results and discussion

Figures 2 and 3 illustrate the impact of the angular and vertical truncated cutoffs (i.e. in terms of M and L), respectively, on the wave excitation volume flux and hydrodynamic coefficients for two coast-integrated OWCs with $R/h = 0.5$, $(R - R_i)/h = 0.1$, $d/h = 0.2$, $D/h = 2.0$ and $\beta = \pi/6$. Similarly, the convergence analysis was carried out for cases with a different number of OWCs and with different OWC geometry. In order to obtain the converged results, $M \geqslant 8$ and $L \geqslant 15$ are suggested. Hereinafter, $M = 12$ and $L = 20$ are adopted.

The present theoretical model is focused on an array of coast-integrated OWCs (i.e. $N \geqslant 2$) without the thin-walled assumption (i.e. $R_i < R$). By contrast, if the OWCs are deployed far away from each other and the thickness of the OWC wall tends to zero (i.e. $R_i \approx R$), the present model could be used to solve the hydrodynamic problems from a thin-walled coast-integrated OWC (i.e. $R_i = R$) approximately, which was investigated by Martins-Rivas & Mei (2009*a*). Figure 4 plots the frequency response of $c_1^{(1)}$ and $a_1^{(1)}$ of the coast-integrated OWC(s) with $R/h = 0.5$ and $d/h = 0.2$. The present results with $N = 2$, $R_i/h = 0.49$, i.e. $(R - R_i)/R = 0.02$, and $D/h = 200$ are in good agreement with those of a single coast-integrated OWC under the thin-wall restriction (Martins-Rivas & Mei 2009*a*).

Additionally, figure 5 illustrates the behaviour of $\bar{c}_1^{(1)}$ and $\bar{c}_2^{(1)}$ versus the non-dimensional wavenumber kh for two coast-integrated OWCs with $R/h = 0.5$, $(R - R_i)/h = 0.1$, $d/h = 0.2$ and $D/h = 2.0$. The plotted results of $\bar{c}_1^{(1)}$ and $\bar{c}_2^{(1)}$

https://doi.org/10.1017/jfm.2019.656 Published online by Cambridge University Press

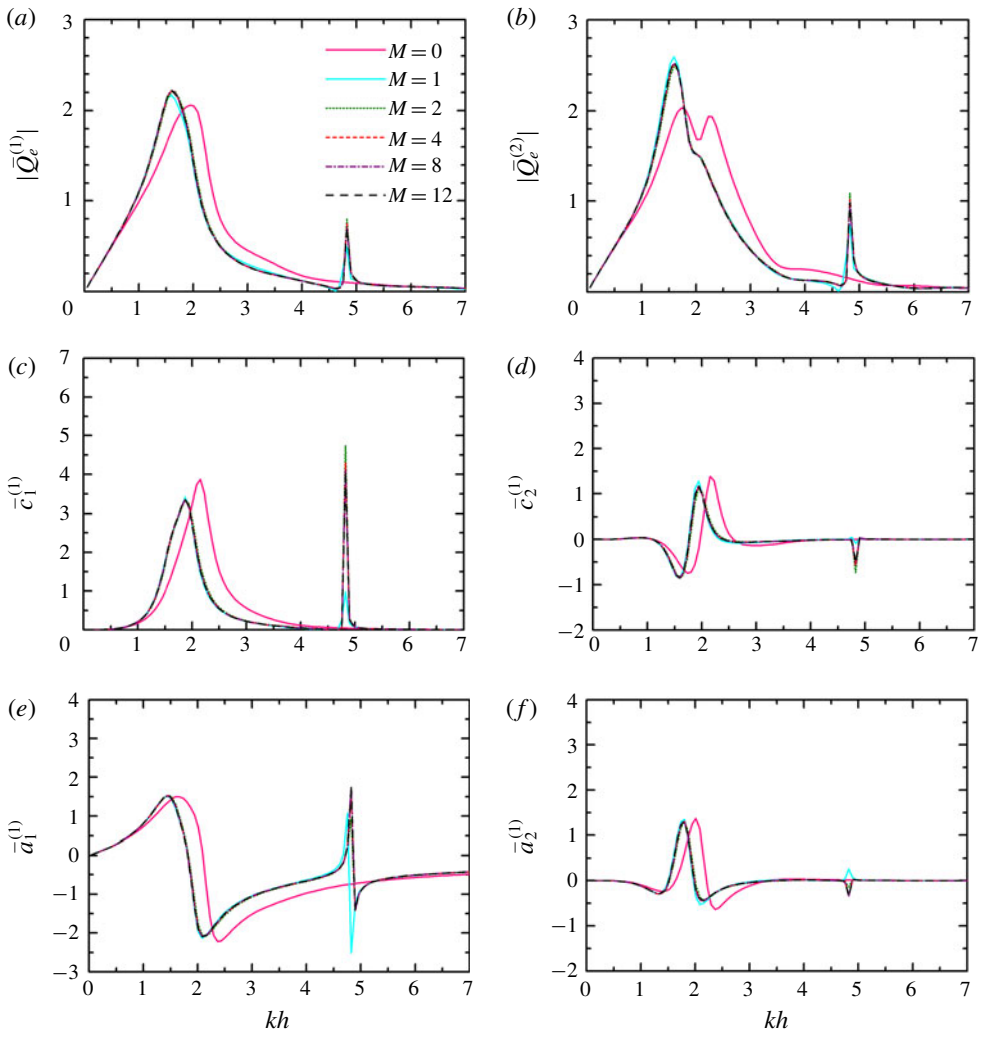


FIGURE 2. (Colour online) Impact of the angular cutoffs (i.e. in terms of M) on wave excitation volume flux and hydrodynamic coefficients, $N = 2$, $R/h = 0.5$, $(R - R_i)/h = 0.1$, $d/h = 0.2$, $D/h = 2.0$, $\beta = \pi/6$ and $L = 20$: (*a*) $|\bar{Q}_e^{(1)}|$; (*b*) $|\bar{Q}_e^{(2)}|$; (*c*) $\bar{c}_1^{(1)}$; (*d*) $\bar{c}_2^{(1)}$; (*e*) $\bar{a}_1^{(1)}$; and (*f*) $\bar{a}_2^{(1)}$.

obtained using the direct method and the Haskind relation cannot be distinguished. This excellent agreement between them, together with the results in figure 4, indicate the accuracy of separate computations of scattering and radiation potentials.

As displayed in figure 5(*a*), there are two peaks of $\bar{c}_1^{(1)}$ ($kh = 1.88$ and 4.82) in the computed range of kh. Figure 6 presents the free-surface patterns ($\mathrm{Re}(\xi_1 \mathrm{e}^{-\mathrm{i}\omega t})/A = \mathrm{Re}(\mathrm{i}\omega p_1 \Phi_1 \mathrm{e}^{-\mathrm{i}\omega t}/g)/A$) in- and outside the two OWC chambers corresponding to these two peaks of $\bar{c}_1^{(1)}$. Owing to the existence of the coast, the opening of each coast-integrated OWC is asymmetrical; as a result, in addition to the Helmholtz mode (the so-called pumping mode), another mode (i.e. the so-called sloshing mode) of the OWC is excited. As shown in figure 6(*a*), the pumping mode dominates the wave

https://doi.org/10.1017/jfm.2019.656 Published online by Cambridge University Press

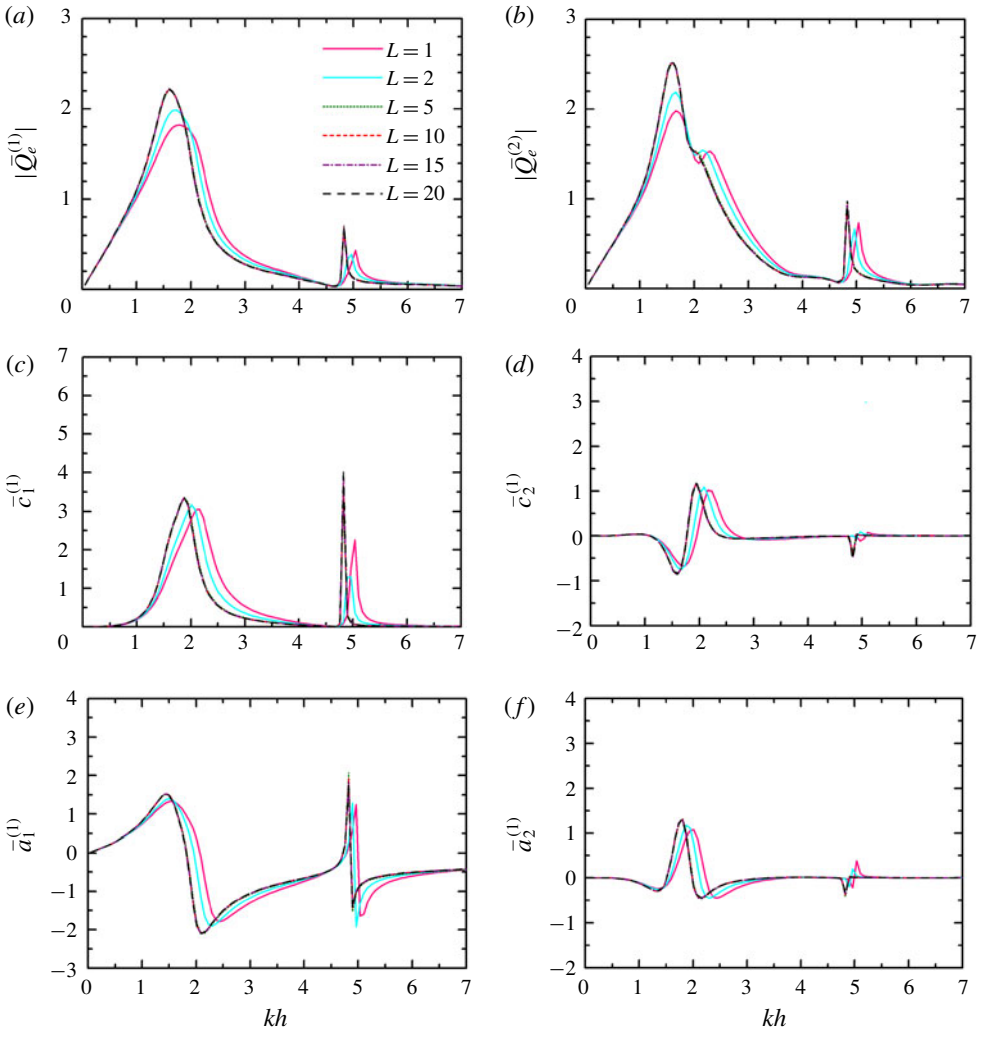


FIGURE 3. (Colour online) Impact of the vertical cutoffs (i.e. in terms of L) on wave excitation volume flux and hydrodynamic coefficients, $N = 2$, $R/h = 0.5$, $(R - R_i)/h = 0.1$, $d/h = 0.2$, $D/h = 2.0$, $\beta = \pi/6$ and $M = 12$: (*a*) $|\bar{Q}_e^{(1)}|$; (*b*) $|\bar{Q}_e^{(2)}|$; (*c*) $\bar{c}_1^{(1)}$; (*d*) $\bar{c}_2^{(1)}$; (*e*) $\bar{a}_1^{(1)}$; and (*f*) $\bar{a}_2^{(1)}$.

motion inside each OWC chamber for $kh = 1.88$. For $kh = 4.82$, as can be seen from figure 6(*b*), the wave motion inside the OWC chambers is dominated by the sloshing mode.

As illustrated in figure 5, compared to the lower peak of $\bar{c}_1^{(1)}$ ($kh = 1.88$), the higher one ($kh = 4.82$) is sharper and much narrower. Here, as given in figure 7, $kh = 1.88$ is taken as an example to present the scattering results of the free-surface patterns ($\mathrm{Re}(\xi_0 \mathrm{e}^{-\mathrm{i}\omega t})/A = \mathrm{Re}(\mathrm{i}\omega\Phi_0 \mathrm{e}^{-\mathrm{i}\omega t}/g)/A$) in- and outside the OWC chambers under incident waves with different angles of incidence: $\beta = \pi/6,\ \pi/4,\ \pi/3$ and $\pi/2$. Despite the fact that, generally speaking, the scattering wave motion around the integrated OWCs depends on the incident wave direction, the motion inside the OWC chambers is dominated by the pumping mode for $kh = 1.88$, regardless of the incident

https://doi.org/10.1017/jfm.2019.656 Published online by Cambridge University Press

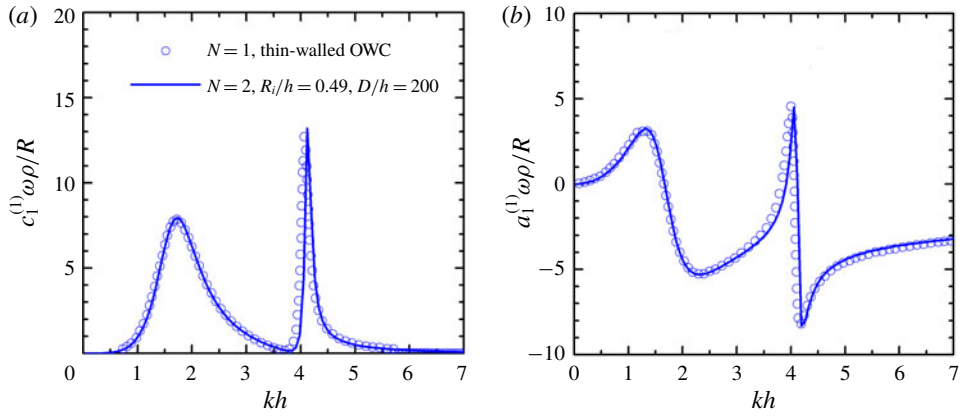


FIGURE 4. (Colour online) Frequency response of $c_1^{(1)}$ and $a_1^{(1)}$ of the coast-integrated OWC(s) with $R/h = 0.5$ and $d/h = 0.2$: (*a*) $c_1^{(1)}$; and (*b*) $a_1^{(1)}$. Circles: results from Martins-Rivas & Mei (2009*a*) for a thin-walled OWC, i.e. $R_i = R$; lines: present results for two OWCs far away from each other.

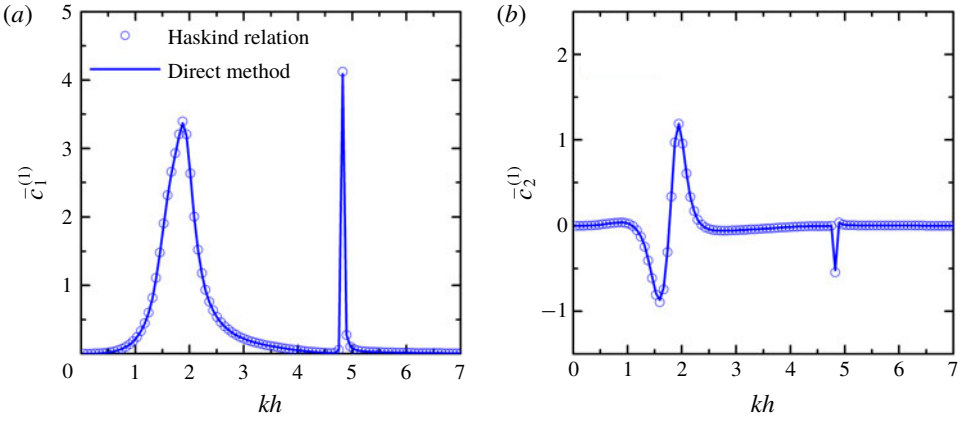


FIGURE 5. (Colour online) Results of wave damping coefficients by using the direct method and the indirect method based on the Haskind relation, $N = 2$, $R/h = 0.5$, $(R - R_i)/h = 0.1$, $d/h = 0.2$ and $D/h = 2.0$: (*a*) $\bar{c}_1^{(1)}$; and (*b*) $\bar{c}_2^{(1)}$.

wave direction (figure 7). Although the sloshing mode plays a rather weak role for such a wave condition, it can still be observed from figure 7 that the symmetrical axis of that mode tends to align itself with the incident wave direction. For $\beta = \pi/2$, as expected, the two water columns behave the same due to the symmetry of both OWC geometry and wave field.

5.1. *Comparison between multiple and single coast-integrated/offshore OWCs*

Figure 8 displays the frequency responses of the hydrodynamic coefficients for two coast-integrated OWCs, the same OWCs in the open sea and a single coast-integrated/offshore OWC (Zheng *et al.* 2018, 2019). For all four cases in the full range of kh, $\bar{c}_1^{(1)}$ is positive (figure 8*a*), which is reasonable from the perspective of

https://doi.org/10.1017/jfm.2019.656 Published online by Cambridge University Press

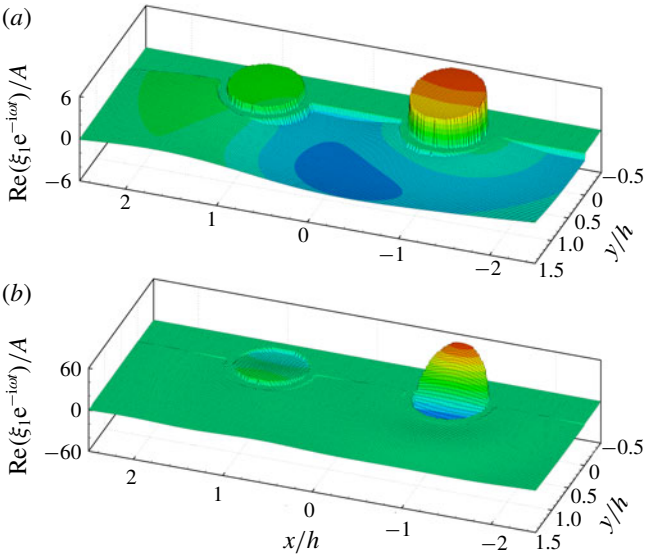


FIGURE 6. (Colour online) Radiation problem: free-surface elevation inside and around the coast-integrated OWCs, $N = 2$, $R/h = 0.5$, $(R - R_i)/h = 0.1$, $d/h = 0.2$, $D/h = 2.0$, $p_1 = \rho g A$ and $p_2 = 0$: (*a*) $kh = 1.88$ at $t = 3\pi/2\omega$; and (*b*) $kh = 4.82$, at $t = \pi/2\omega$.

energy conservation and outgoing propagation of radiated waves (Zheng & Zhang 2018). For both the single and two offshore OWC(s) cases, there is only one peak of the $\bar{c}_1^{(1)}$–kh curve at $kh = 2.44$ in the computed range of kh, which corresponds to a pumping mode. The peak value of $\bar{c}_1^{(1)}$ for the two offshore OWCs is somewhat larger than that of the single offshore OWC due to the hydrodynamic interaction between them. For the single/two coast-integrated OWC(s) cases, two modes are excited – the lower (around $kh = 1.85$) dominated by the pumping mode, the higher (at $kh = 4.82$) dominated by the sloshing mode. Owing to the constraint of the coastline, the wave motion inside the OWC chamber is more restricted compared to that of the offshore cases, leading to smaller peaks of $\bar{c}_1^{(1)}$. As can be seen from figure 8(*c*), the corresponding $\bar{a}_1^{(1)}$ parameter changes its sign rapidly around those kh values where the peaks of $\bar{c}_1^{(1)}$ occur. Since the effect of hydrostatic stiffness has already been included in $\bar{a}_1^{(1)}$, the kh values where $\bar{a}_1^{(1)}$ vanishes correspond to natural resonance. The light grey line plotted in figure 8(*c*) represents $-\bar{a}_{PTO}$, which is induced by the air compressibility. When taken into account, resonance happens at the kh values where the $\bar{a}_1^{(1)}$ and $-\bar{a}_{PTO}$ curves intersect each other. For the two offshore/coast-integrated OWCs (figure 8*b*,*d*), the ranges of $\bar{c}_2^{(1)}$ and $\bar{a}_2^{(1)}$ are comparable to those of $\bar{c}_1^{(1)}$ and $\bar{a}_1^{(1)}$, indicating the significant influence of the hydrodynamic interaction between multiple OWCs.

The frequency responses of the wave excitation volume flux in terms of the amplitude and phase for these four cases subjected to incident waves with $\beta = \pi/2$ are plotted in figure 9. The basic shapes of the $|\bar{Q}_e^{(1)}|$–kh curves (figure 9*a*) look similar to those of $\bar{c}_1^{(1)}$–kh (figure 8*a*). However, due to the wave reflection from the vertical coastline, the peaks of $|\bar{Q}_e^{(1)}|$ for the coast-integrated OWC(s) are larger than those of offshore situations, and clearly shift towards lower frequencies. The shift of the position of the peaks can be explained from the point of view of the natural

https://doi.org/10.1017/jfm.2019.656 Published online by Cambridge University Press

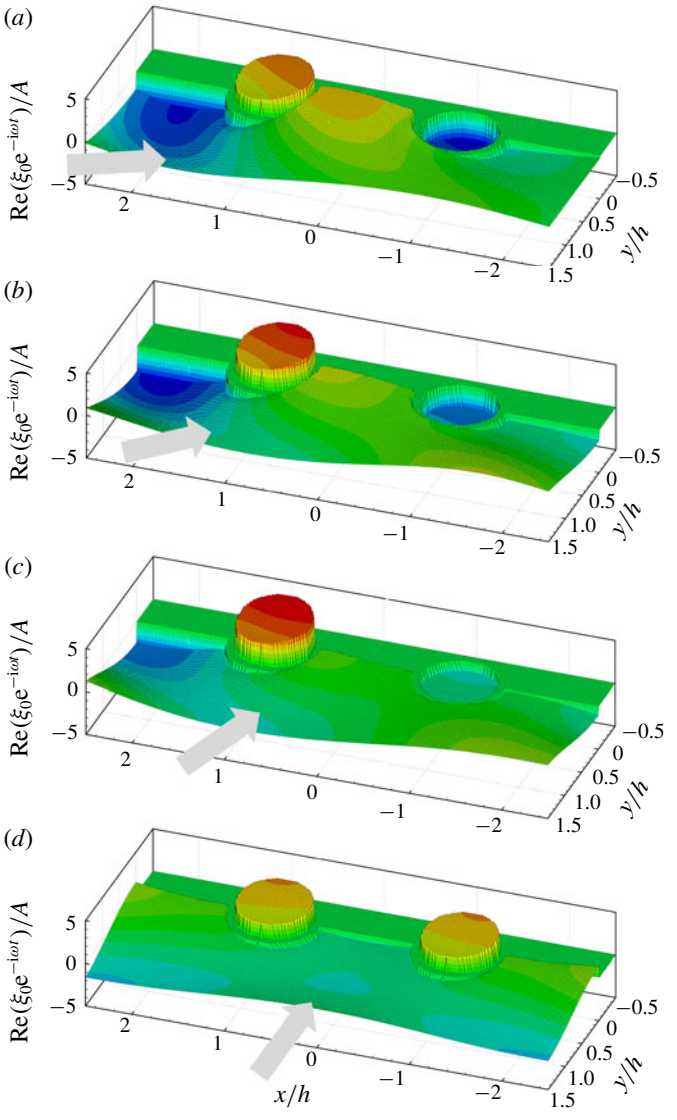


FIGURE 7. (Colour online) Scattering problem: free-surface elevation inside and around the coast-integrated OWCs, $N=2$, $R/h=0.5$, $(R-R_i)/h=0.1$, $d/h=0.2$, $D/h=2.0$, $t=0$ and $kh=1.88$: (*a*) $\beta=\pi/6$; (*b*) $\beta=\pi/4$; (*c*) $\beta=\pi/3$; and (*d*) $\beta=\pi/2$.

modes: compared to the offshore OWC(s), for which the space under the chamber wall is entirely open to the water, in the case of the coast-integrated OWC(s), half of the space below the chamber on the coast side is closed, implying that a greater proportion of the water column is enclosed. This leads to smaller natural frequencies and, therefore, the OWC(s) are more likely to be significantly excited at lower frequencies. The peaks of $|\bar{Q}_e^{(1)}|$ for the two OWCs, regardless of whether they are coast-integrated or offshore, can benefit from the hydrodynamic interaction between them, e.g. the peak value of $|\bar{Q}_e^{(1)}|$ of 2.69 for the single coast-integrated OWC, which is reached for $kh=1.73$, is enhanced to 3.64 for the two coast-integrated OWCs, and

https://doi.org/10.1017/jfm.2019.656 Published online by Cambridge University Press

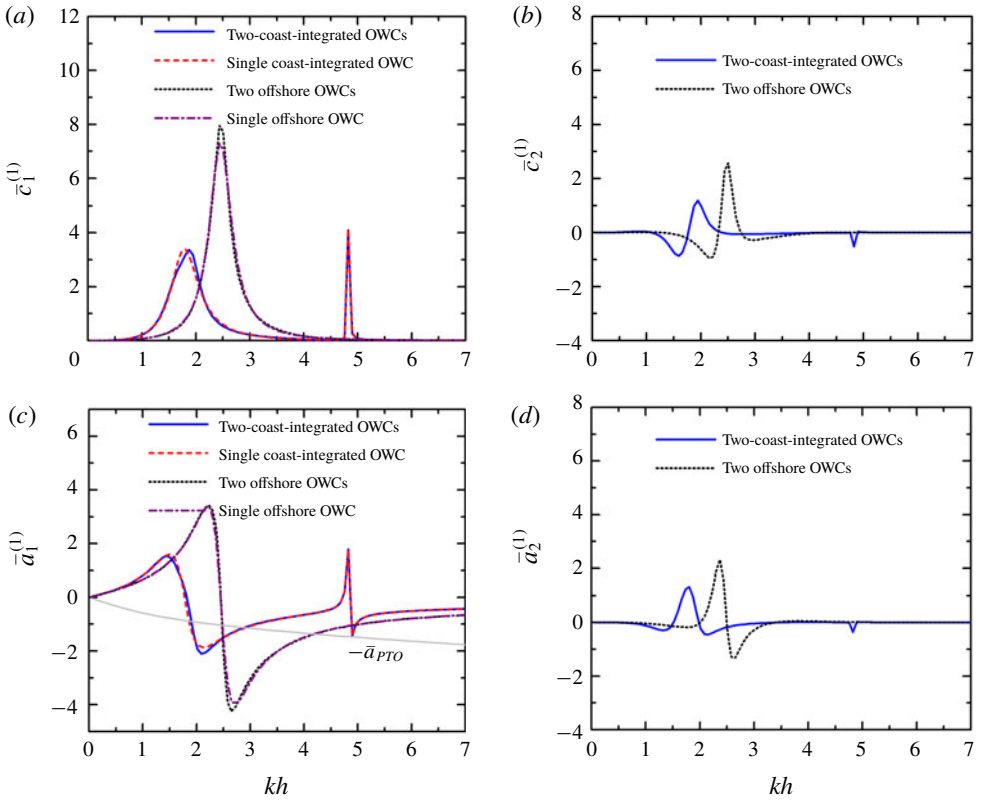


FIGURE 8. (Colour online) Radiation problem, $R/h = 0.5$, $(R - R_i)/h = 0.1$, $d/h = 0.2$, $D/h = 2.0$ and $h = 10$ m: (*a*) $\bar{c}_1^{(1)}$; (*b*) $\bar{c}_2^{(1)}$; (*c*) $\bar{a}_1^{(1)}$ and $-\bar{a}_{PTO}$; and (*d*) $\bar{a}_2^{(1)}$.

occurs at $kh = 1.88$. In long waves, e.g. $kh < 1.5$, the size of the OWCs is small compared to the wavelength, so that the primary effect on the wave field is reflection at the coast, leading to an overlapping of $\varphi_e^{(1)}$–kh for the single/two OWC(s) cases and a separation for offshore and coast-integrated situations (figure 9*b*).

The wave power extraction from these four cases of OWC(s) are displayed in figure 10 in terms of power capture factor, array factor, coast factor and PTO damping employed. The curve of $-\bar{a}_{PTO}$ intersects the curve of $\bar{a}_1^{(1)}$ at two values of kh, i.e. 2.47 and 4.19, in the computed range of kh for single/two offshore OWC(s) (see figure 8*c*), and the corresponding wave capture factors (η' and η_0') as shown in figure 10(*a*) also attain their optimum at these two wave frequencies. The value of η_0' is exactly 1.0 at the resonant frequencies displayed, which is reasonable and can be theoretically derived by using the Haskind relation (e.g. Falnes 2002). For the two offshore OWCs case, the largest value of the wave capture factor (η' as displayed in figure 10*a*) can reach 2.27. There is an obvious drop in η' between these two resonant frequencies, for $kh \in (3.0, 3.5)$, implying that the two OWCs cannot continuously capture wave power effectively in a large range of kh. When the OWC(s) is(are) integrated into a coast, three intersections of $\bar{a}_1^{(1)}$ and $-\bar{a}_{PTO}$ occur, at $kh = 1.88$, 2.92 and 4.82 (figure 8*c*), resulting in three peaks of η and η_0 (figure 10*a*). Compared to those of the offshore cases, although the first two resonant frequencies of the coast-integrated cases are closer to each other, η_0 remains mostly around 2.0 for kh between these two frequencies, leading to an even broader

https://doi.org/10.1017/jfm.2019.656 Published online by Cambridge University Press

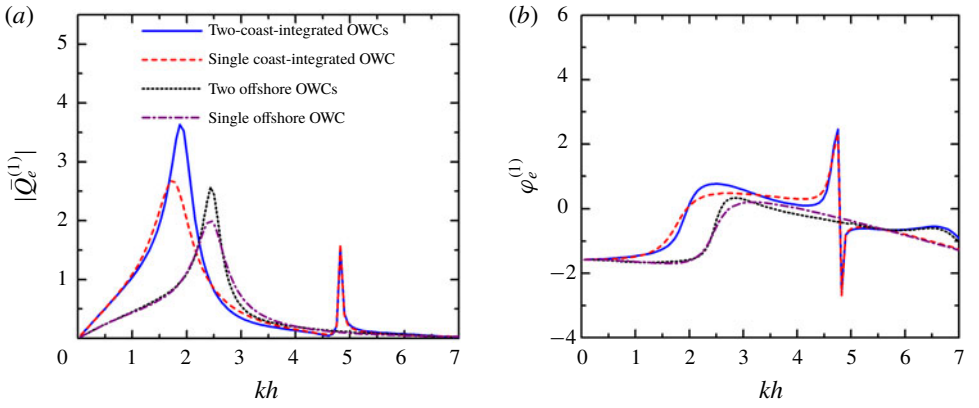


FIGURE 9. (Colour online) Scattering problem, $R/h = 0.5$, $(R - R_i)/h = 0.1$, $d/h = 0.2$, $D/h = 2.0$ and $\beta = \pi/2$: (*a*) amplitude of wave excitation volume flux, $|\bar{Q}_e^{(1)}|$; and (*b*) phase of wave excitation volume flux, $\varphi_e^{(1)}$.

bandwidth of high efficiency. For the two coast-integrated OWCs, thanks to the constructive hydrodynamic interaction between them, a large peak value of η, 6.46, is achieved around $kh = 1.88$. The corresponding $\bar{c}_{PTO}$ (figure 10*b*) shows that, in order to reach optimum efficiency for all wave conditions, the turbine parameter for the coast-integrated cases does not need to be varied as much as that in the offshore cases, making it relatively easy to achieve in practice.

The variation of the array factor for the coast-integrated and offshore cases (i.e. q and q') with kh (figure 10*c*) indicates that both q and q' tend to unity as kh tends to 0. As a comparison, the coast reflection effect factor for single/two coast-integrated cases (i.e. q_c and $q_{c,0}$, figure 10*d*) tends to 4.0 when kh tends to 0. This is due to the fact that incident waves are the dominant element in the excitation volume flux under long waves. In the open sea, the amplitude of undisturbed incident waves is A, whereas the amplitude of incident waves subjected to reflection from the vertical coast turns out to be $2A$, leading to a doubling of the excitation volume flux and, in turn, affecting wave power extraction. For short waves, e.g. $kh > 5.5$, the curves of q and q' tend to overlap each other and the values of q_c and $q_{c,0}$ both approach unity. This can be explained by the dominant role of $\bar{c}_{PTO}$ and $\bar{a}_{PTO}$ in the wave power capture factor (refer to (4.5)) in short wave conditions. For $kh > 6.0$, all hydrodynamic coefficients vanish alongside the wave excitation volume flux (figures 8–10), whereas $\bar{c}_{PTO}$ and $\bar{a}_{PTO}$ remain non-vanishing and become even larger with the increase of kh. As displayed in figure 10(*d*), for most wave conditions, except $kh \in (3.5, 4.8)$ and $kh > 5.5$, the coast factors remain far above unity, indicating a constructive effect of coast reflection on wave power absorption. However, the array factor oscillates around 1.0 and shows alternating constructive and destructive effects with the change of kh (figure 10*c*). In the following sections, only the wave capture factor and array factor are preserved to indicate power extraction of the coast-integrated OWCs. As can be seen from figure 10(*a*,*c*,*d*), the dramatic peak of η occurring at $kh = 1.88$ benefits from both the constructive array effect ($q = 1.5$) and the constructive coast effect ($q_c = 6.0$).

5.2. *Effect of incident wave direction*

The wave excitation volume flux of each OWC, the power capture factor of each OWC and both together with the q-factor for different incident wave directions β

https://doi.org/10.1017/jfm.2019.656 Published online by Cambridge University Press

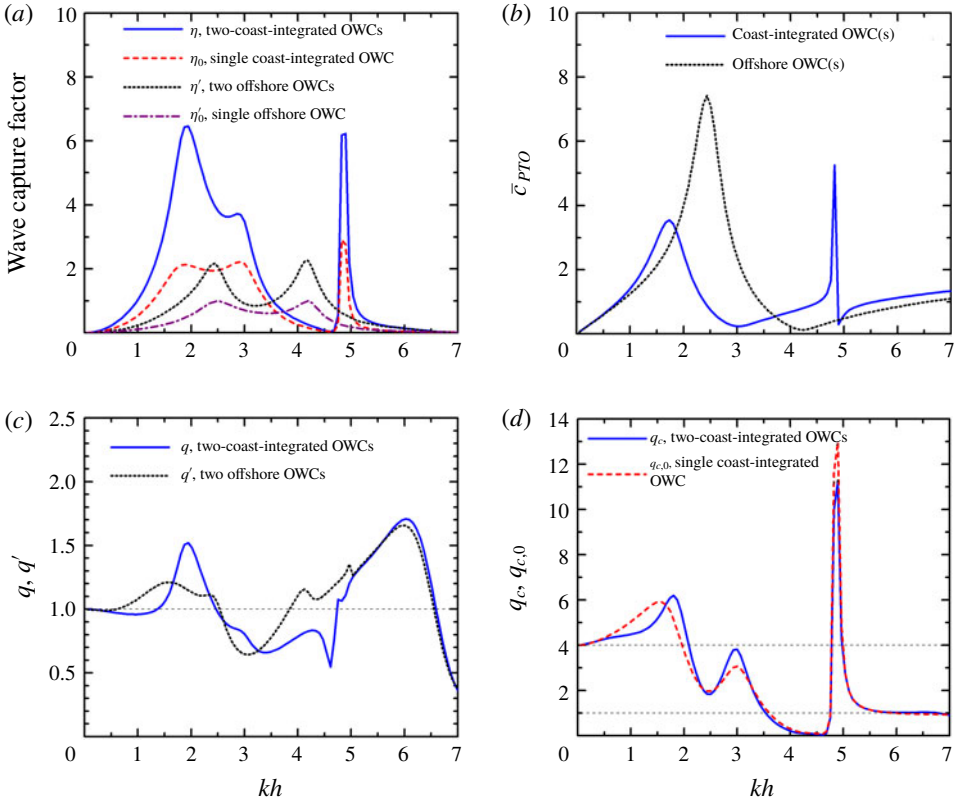


FIGURE 10. (Colour online) Power extraction, $R/h = 0.5$, $(R - R_i)/h = 0.1$, $d/h = 0.2$, $D/h = 2.0$, $\beta = \pi/2$ and $h = 10$ m: (*a*) wave capture factor, η, η_0, η' and η'_0; (*b*) $\bar{c}_{PTO}$; (*c*) array factor, q and q'; and (*d*) coast factor, q_c and $q_{c,0}$.

are displayed in figure 11. As β increases from $\pi/6$ to $\pi/2$, the main peak of the wave excitation volume flux of the up-wave OWC ($|\bar{Q}_e^{(2)}|$) becomes larger and shifts towards large kh. The first peak for the other OWC ($|\bar{Q}_e^{(1)}|$), on the contrary, first falls and shifts towards small kh, and then rises and shifts in the opposite direction rapidly to the same position of $|\bar{Q}_e^{(2)}|$ for $\beta = \pi/2$. Note that, at $kh \approx 2.0$, a slight rise of the $|\bar{Q}_e^{(1)}|$ or $|\bar{Q}_e^{(2)}|$ curves with specified values of β is observed, e.g. more particularly, an additional peak of the $|\bar{Q}_e^{(1)}|$–kh curve for $\beta = \pi/3$ can be excited. This appears to be induced by the resonance of water waves between the two OWCs, for $k(D - R) \approx \pi$ is satisfied for these cases at $kh \approx 2.0$. For $\beta = \pi/6$ and $\pi/4$, the wave power capture factor of the up-wave OWC (η_2) is generally larger than the down-wave one (η_1) for $kh \in (1.5, 3.5)$ (figure 11*b*), whereas for $\beta = \pi/3$, $\eta_1 > \eta_2$ is observed for $kh \in (2.0, 3.0)$. As displayed in figure 11(*c*), for $kh \in (1.5, 2.0)$, the overall power capture factor (η) increases dramatically with the increase of β from $\pi/6$ to $\pi/2$. For $kh \in (2.6, 4.0)$, the η corresponding to $\beta = \pi/3$ is significantly greater than those for all three other incident wave directions, including $\beta = \pi/2$. This can be explained from the perspective of the array effect as illustrated in figure 11(*d*), in which constructive ($q > 1.0$) and destructive ($q < 1.0$) effects are indicated for $\beta = \pi/3$ and $\pi/2$, respectively, for $kh \in (2.6, 4.0)$. The following sections focus on the cases with $\beta = \pi/2$.

https://doi.org/10.1017/jfm.2019.656 Published online by Cambridge University Press

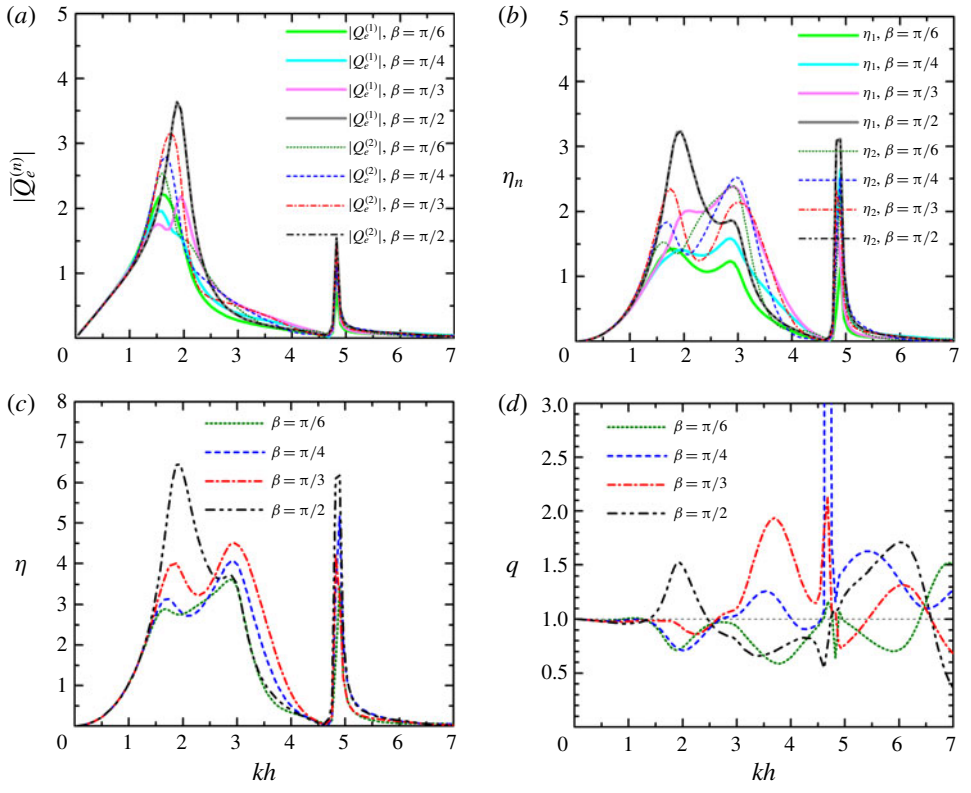


FIGURE 11. (Colour online) Comparison for different incident direction, β, with $N = 2$, $R/h = 0.5$, $(R - R_i)/h = 0.1$, $d/h = 0.2$, $D/h = 2.0$ and $h = 10$ m: (*a*) $|\bar{Q}_e^{(n)}|$; (*b*) η_n; (*c*) η; and (*d*) q-factor.

Note that, at $kh = 1.88$, the maximum η for $\beta = \pi/2$ is dramatically higher than 4.0, while the η values for $\beta = \pi/6$ and $\pi/4$ are obviously lower than 4.0. Instead, at $kh = 2.92$, the η values for the four cases with different values of β are all concentrated around 4.0. In fact, for any certain wave frequency, there is a general identity of the optimum wave capture factor (η_{MAX}) over all incidence angles that multiple coast-integrated OWCs must hold regardless of the OWC dimension, i.e.

$$\frac{1}{\pi}\int_0^{\pi} \eta_{MAX}(\beta)\,\mathrm{d}\beta = 2N, \tag{5.1}$$

which can be theoretically confirmed by invoking the ideal optimization criteria and the Haskind relation (Wolgamot, Taylor & Taylor 2012). A detailed derivation is given in appendix B.

5.3. *Effect of radius of the OWCs*

The effect of radius (R/h) of the OWCs on wave excitation volume flux, hydrodynamic coefficients, wave capture factor and array factor were investigated (figure 12). As R/h increases from 0.3 to 0.7, the main peak of the $|\bar{Q}_e^{(n)}|$ curve, as shown in figure 12(*a*), shifts towards lower frequencies and tends to be flatter. The peak value first becomes larger and then smaller after reaching the largest value with $R/h = 0.5$. As illustrated

https://doi.org/10.1017/jfm.2019.656 Published online by Cambridge University Press

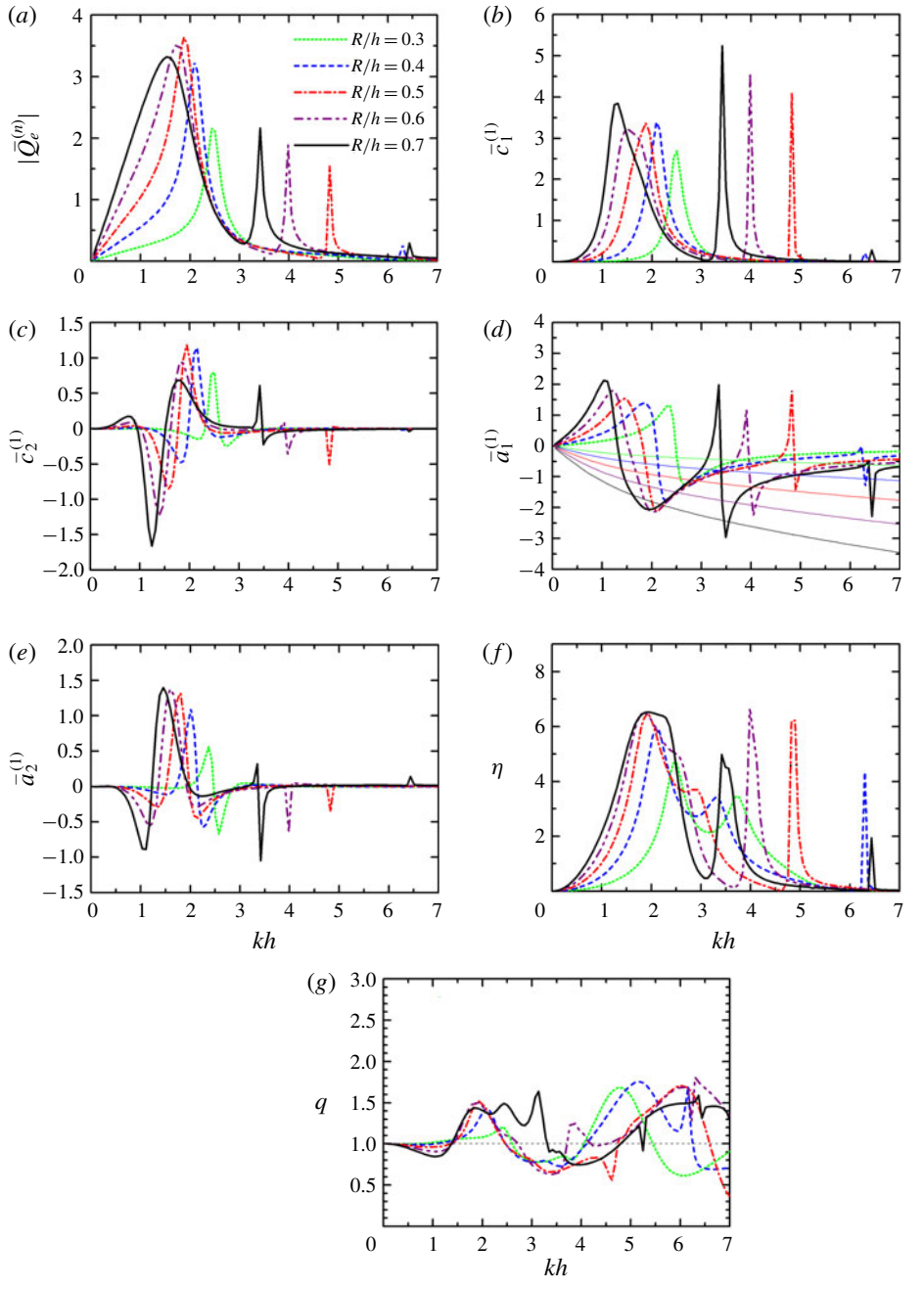


FIGURE 12. (Colour online) Comparison for different radius of the OWCs, R/h, with $N = 2$, $(R - R_i)/h = 0.1$, $d/h = 0.2$, $D/h = 2.0$, $\beta = \pi/2$ and $h = 10$ m: (*a*) $|\bar{Q}_e^{(n)}|$; (*b*) $\bar{c}_1^{(1)}$; (*c*) $\bar{c}_2^{(1)}$; (*d*) $\bar{a}_1^{(1)}$ and $-\bar{a}_{PTO}$ (solid thin curves in the same colour of $\bar{a}_1^{(1)}$ for the same value of R/h); (*e*) $\bar{a}_2^{(1)}$; (*f*) η; and (*g*) q-factor.

https://doi.org/10.1017/jfm.2019.656 Published online by Cambridge University Press

in figure 12(*b*), for the smallest column $R/h = 0.3$, the curve of $\bar{c}_1^{(1)}$ has only one peak in the computed range of kh. For larger R/h, i.e. $R/h = 0.4$–0.6 and $R/h = 0.7$, two and three peaks, are evident, respectively. This is associated with the natural resonance modes (without PTO system), which are strongly dependent on the relative size of OWC chamber to wavelength. Figure 12(*c*,*e*) indicates that, with the increase of R/h, the oscillation amplitudes of the $\bar{c}_2^{(1)}$ and $\bar{a}_2^{(1)}$ curves become larger, and the kh corresponding to these largest amplitudes get smaller. As previously defined in § 4, $\bar{a}_{PTO}$ depends on the chamber volume $V_0 = \pi R^2 h$, which in turn depends critically on R/h.

In figure 12(*d*), apart from the five curves of $\bar{a}_1^{(1)}$, five solid thin curves of $-\bar{a}_{PTO}$ relating to five different values of R/h are plotted in the corresponding colour. For $R/h = 0.3$, there are two points of interaction between $-\bar{a}_{PTO}$ and $\bar{a}_1^{(1)}$ in the range of kh plotted; while for larger R/h, more points of interaction can be achieved, e.g. four interaction points for $R/h = 0.7$. As R/h increases from 0.3 to 0.7, the curve of $-\bar{a}_{PTO}$ is slanted downwards, resulting in the first two points of interaction moving towards lower frequencies and the horizontal distance between them getting smaller. The kh values corresponding to the points of interaction between $-\bar{a}_{PTO}$ and $\bar{a}_1^{(1)}$ identified from figure 12(*d*) coincide well with the peak positions of the η curves (figure 12*f*). As R/h increases, the main peaks of the η curve shift towards lower kh and gain intensity. Figure 12(*g*) shows that the q-factor remains above unity for $kh \in (1.4, 2.5)$ regardless of the value of R/h. For $R/h = 0.7$, constructive array effects can be obtained for a rather large range of kh, i.e. $kh \in (1.4, 3.3)$. Although some higher and broader peaks of q can be achieved for $kh > 4.5$, they are not attractive, because either η is too small, or η is only large in a narrow bandwidth.

5.4. *Effect of wall thickness of the OWCs*

The theoretical results for the OWCs with different chamber wall thickness are plotted in figure 13. As the wall thickness of the OWC chambers increases, i.e. the inner radius of the chamber decreases while the outer radius remains constant, the main peak of $|\bar{Q}_e^{(n)}|$ shifts slightly towards higher wave frequencies with a narrower bandwidth (figure 13*a*), while its peak height remains approximately the same. A similar change occurs for $\bar{c}_1^{(1)}$ (figure 13*b*), with the main peak becoming higher and more abrupt with the increase of wall thickness of the OWCs. Correspondingly, the first sign changing point of $\bar{a}_1^{(1)}$ (figure 13*d*) occurs at a lower frequency, and its variation in amplitude gets larger, and happens in a narrower range of kh. With the increase of wall thickness, the position of the largest oscillation amplitude of $\bar{c}_2^{(1)}$ and $\bar{a}_2^{(1)}$ (figure 13*c*,*e*) moves towards large kh and the variation becomes more abrupt as well. As illustrated in figure 13(*f*), the peaks of η at $kh \in (1.0, 3.5)$ are lower and the overall bandwidth is narrower for a thicker wall of each OWC chamber. This can also be reflected by the intersections between the $-\bar{a}_{PTO}$ and $\bar{a}_1^{(1)}$ curves (figure 13*d*), which get closer to each other horizontally. In figure 13(*g*), a smaller q-factor is shown to be obtained for the OWCs with a thicker chamber wall for most $kh \in (1.8, 3.5)$, suggesting a relatively more destructive array effect. Hence it may be concluded that, to achieve higher wave power absorption efficiency in a broader bandwidth, the OWC chambers with a thinner wall are more appropriate. It should be noted that in practice the chamber wall should not be so thin as to lose structural robustness.

https://doi.org/10.1017/jfm.2019.656 Published online by Cambridge University Press

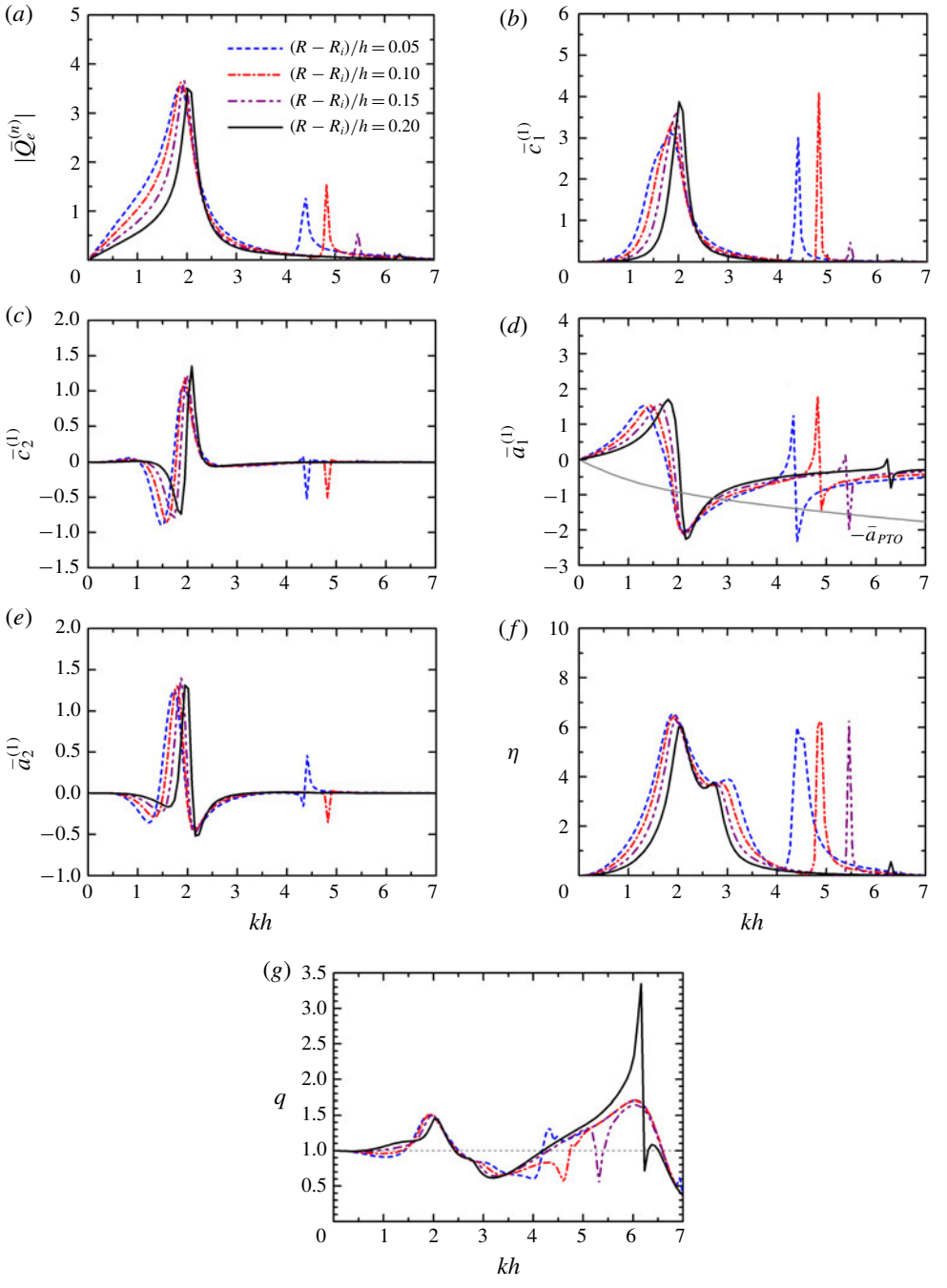


FIGURE 13. (Colour online) Comparison for different wall thickness of the OWCs, $(R-R_i)/h$, with $N=2$, $R/h=0.5$, $d/h=0.2$, $D/h=2.0$, $\beta=\pi/2$ and $h=10$ m: (*a*) $|\bar{Q}_e^{(n)}|$; (*b*) $\bar{c}_1^{(1)}$; (*c*) $\bar{c}_2^{(1)}$; (*d*) $\bar{a}_1^{(1)}$ and $-\bar{a}_{PTO}$; (*e*) $\bar{a}_2^{(1)}$; (*f*) η; and (*g*) q-factor.

https://doi.org/10.1017/jfm.2019.656 Published online by Cambridge University Press

5.5. *Effect of submergence of the OWCs*

The submergence of the chamber, d/h, can also strongly affect the hydrodynamics and power extraction of the coast-integrated OWCs. As indicated in figure 14(*b*,*d*), the peaks of $\bar{c}_1^{(1)}$ and the sign changing points of $\bar{a}_1^{(1)}$ are found to shift towards lower kh with the increase of d/h. This is reasonable, since a larger d/h means a higher, heavier water column enclosed within the chamber, leading to a smaller natural frequency. As d/h increases, the curve of $|\bar{Q}_e^{(n)}|$ becomes more abrupt (figure 14*a*), and the peaks become higher and move towards low kh. As indicated in figure 14(*c*,*e*), the frequencies corresponding to the dramatic variations of $\bar{c}_2^{(1)}$ and $\bar{a}_2^{(1)}$ decrease with increasing d/h. It is worth noting that, with the decrease of d/h, although the peaks of the η curve remain at approximately the same levels (figure 14*f*), there is a distinct movement of these peaks towards large kh, which can be indicated as well from the position changes of the intersections between the $-\bar{a}_{PTO}$ and $\bar{a}_1^{(1)}$ curves (figure 14*d*). Furthermore, broader and smoother peaks of η are achieved for a smaller d/h as shown in figure 14(*f*). For short waves, e.g. $kh \in (5.5, 7.0)$, more power can be captured with the decrease of d/h, and this constructive effect becomes stronger and stronger. This is due to the fact that most wave power (approximately 95 %) is concentrated at no more than one-quarter of a wavelength below the still-water level, where the kinetic energy at a shallower position is more intensive compared to that at a deeper position. For most wave conditions at $kh \in (2.2, 3.6)$, a larger q-factor is obtained for a smaller d/h (figure 14*g*). Therefore, to have a better array effect and ultimately to achieve high power absorption in a rather broader bandwidth, the submergence of the OWC chambers should be as small as possible. However, the realistic chamber submergence cannot be too small, otherwise the opening may not be continuously submerged in the water when the OWCs are subjected to either strong waves or a large tidal range.

5.6. *Effect of distance between the OWCs*

Figure 15 presents the effect of distance between the OWCs. Similar results for the individually isolated single coast/breakwater-integrated OWC (denoted as 'isolated') are also displayed for comparison. Figure 15(*a*) shows that there are two peaks of the $|\bar{Q}_e^{(n)}|$–kh curve over the computed range of kh, with the main one around $kh \approx 1.8$ and the second sharp one at a higher frequency, i.e. $kh \approx 4.82$. As D/h increases from 1.5 to 3.0, the amplitude of the main peak first increases and then decreases. Although the amplitude of the main peak for $D/h = 1.5$ is merely 2.4, large values of $|\bar{Q}_e^{(n)}|$ compared to the other cases are obtained at $kh \in (2.1, 3.0)$. The kh corresponding to the main peak shifts towards lower frequencies. The second sharp peak is nearly independent of D/h. As shown in figure 15(*b*,*d*), a rather limited impact of D/h on $\bar{c}_1^{(1)}$ and $\bar{a}_1^{(1)}$ is observed at $kh \in (1.5, 2.5)$, where the main peak of the $\bar{c}_1^{(1)}$–kh curve and the corresponding drop of $\bar{a}_1^{(1)}$ occur. As D/h varies, the $\bar{c}_1^{(1)}(\bar{a}_1^{(1)})$–$kh$ curve of the two OWCs oscillates slightly around that of the 'isolated' case. This is due to the fact that the waves radiated from each coast/breakwater-integrated OWC, and also those waves diffracted from the other OWC, act on the OWC in question simultaneously. The change in D/h leads to alteration of the phase difference between the two-OWCs mutual radiated and diffracted waves, resulting in the switch of reinforcing and diminishing influences. The amplitudes of the peak of $\bar{c}_1^{(1)}$ and the drop of $\bar{a}_1^{(1)}$ at $kh = 1.8$ are both approximately 3.5.

As a comparison (figure 15*c*,*e*), the variations of $\bar{c}_2^{(1)}$ and $\bar{a}_2^{(1)}$, especially for $kh \in (1.0, 3.0)$, are significantly dependent upon D/h. The amplitudes of the drops of $\bar{c}_2^{(1)}$

https://doi.org/10.1017/jfm.2019.656 Published online by Cambridge University Press

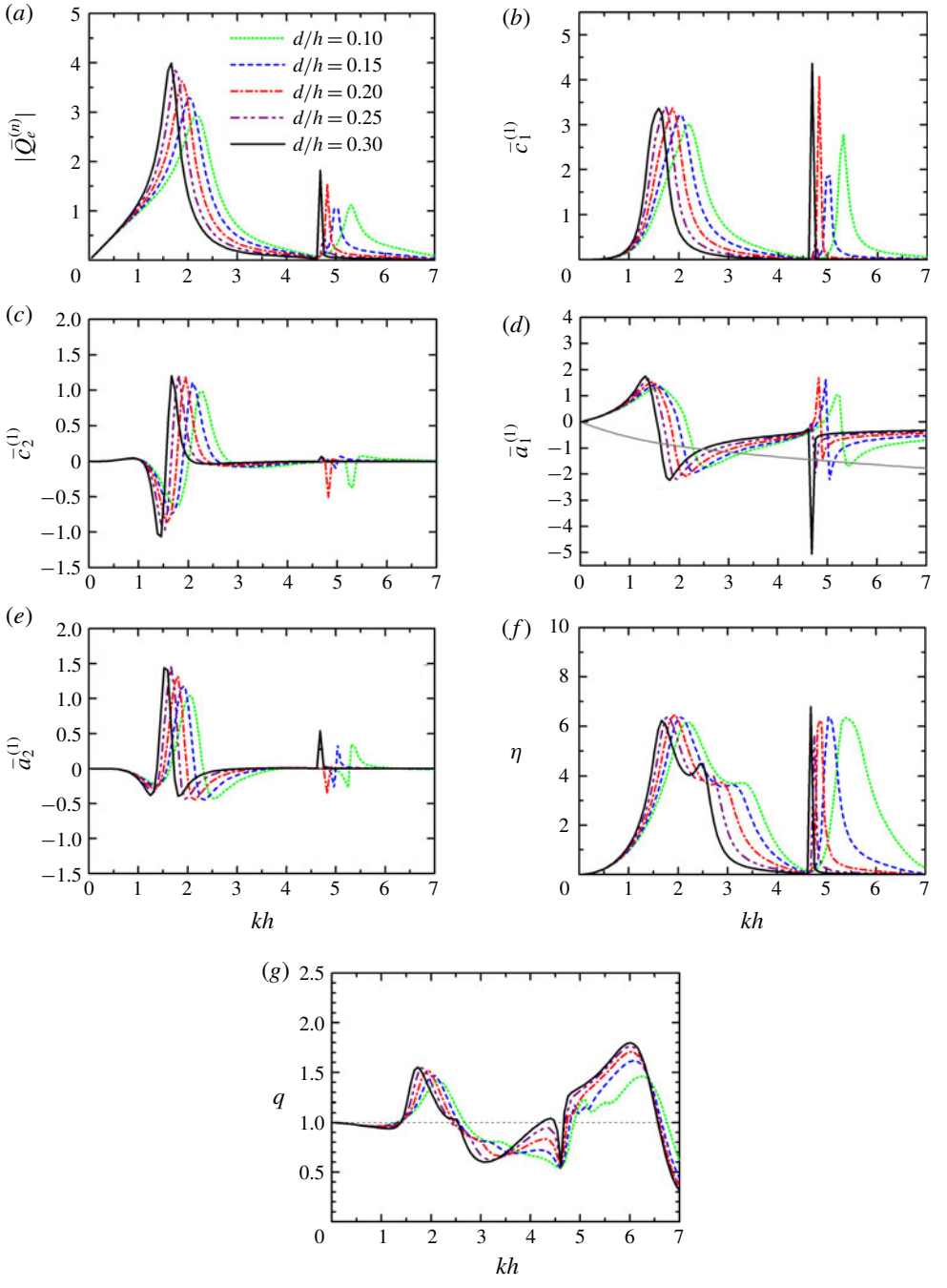


FIGURE 14. (Colour online) Comparison for different submergence of the OWCs, d/h, with $N = 2$, $R/h = 0.5$, $(R - R_i)/h = 0.1$, $D/h = 2.0$, $\beta = \pi/2$ and $h = 10$ m: (*a*) $|\bar{Q}_e^{(n)}|$; (*b*) $\bar{c}_1^{(1)}$; (*c*) $\bar{c}_2^{(1)}$; (*d*) $\bar{a}_1^{(1)}$ and $-\bar{a}_{PTO}$; (*e*) $\bar{a}_2^{(1)}$; (*f*) η; and (*g*) q-factor.

https://doi.org/10.1017/jfm.2019.656 Published online by Cambridge University Press

and $\bar{a}_2^{(1)}$ around $kh = 1.8$ are both found to be no smaller than 1.6, revealing a strong hydrodynamic interaction between the OWCs for the four cases of D/h examined. As D/h increases from 1.5 to 3.0, these drops of $\bar{c}_2^{(1)}$ and $\bar{a}_2^{(1)}$ become progressively weaker, and it can be expected that, for $D/h \to \infty$, $\bar{c}_2^{(1)} \approx 0$ and $\bar{a}_2^{(1)} \approx 0$ will be obtained. The wave power capture factor of the 'isolated' case, i.e. η_0, is no more than 2.0 (figure 15*f*). However, for the cases consisting of two OWCs, the value of $\eta > 6.0$ can be obtained for certain values of D/h due to hydrodynamic interactions. From the perspective of the peak value of η, the OWCs with $D/h = 2.0$ could be the best solution for power absorption. However, in practice, the OWCs with $D/h = 1.5$ might be a better choice for their good performance over a broader bandwidth, with a sufficiently large wave capture factor. It can be learned (figure 15*g*) that, indeed, the D/h ratio has a strong effect on the shape of the q-factor curve as well as on its amplitude. For $D/h = 1.5$, $q > 1.0$ is satisfied at $kh \in (1.8, 3.4)$, meaning that a constructive hydrodynamic interaction between the OWCs is achieved in a large range of wave conditions.

5.7. *Effect of the number of OWCs*

The frequency responses of the wave power capture factor of each OWC for $N = 2$, 3, 4 and 5, together with the overall q-factor, are plotted in figure 16. The wave power capture factor of the isolated single coast/breakwater-integrated OWC (i.e. η_0) are also displayed as a comparison. Since the OWCs with the same size are uniformly distributed along the straight coast and are subjected to incident waves with $\beta = \pi/2$, the performance of an individual OWC is the same as the one symmetrical about the centrosymmetric plane of the OWC array. For the sake of simplicity, only the results of the first half number of OWCs are displayed, including the middle one as well if N is odd. It is shown in figure 16(*a–d*) that, from the perspective of the peak value of the power capture factor, the performance of each OWC among the multiple OWCs is better than that of the single isolated coast-integrated OWC. The closer the OWC is to the middle position of the array, the higher its peak power capture factor. For other wave conditions rather than the peak frequencies, e.g. $kh \in (2.8, 3.5)$, less power can be extracted by an OWC in an array of OWCs, compared to the single isolated coast-integrated case. Moreover, much less can be captured by the OWC closer to the middle position of the array. This tendency of the performances of an array of OWCs compared to a single OWC can also be clearly detected from the q-factor as plotted in figure 16(*e*). For $kh \in (2.0, 2.5)$, although $q > 1$ is achieved for all the examples considered, the q value for two OWCs is obviously smaller than those with more OWCs. It might be concluded that for such a range of wave conditions, an array of coast-integrated OWCs consisting of three or more OWCs could be a better choice, to benefit more fully from array effects, and in turn to extract wave power more efficiently.

5.8. *Effect of the distance difference*

We consider the effect of varying the distances on wave power extraction from five coast-integrated OWCs subjected to incident waves with $\beta = \pi/2$. The overall length of the array is fixed as $D_1 + D_2 + D_3 + D_4 = 8h$ and the OWCs are symmetrically deployed about the central OWC, i.e. $D_1 = D_4$, $D_2 = D_3$. Seven cases with $(D_2 - D_1)/h = \Delta D/h = -1.5$, -1.0, -0.5, 0, 0.5, 1.0 and 1.5 are examined. Figure 17 presents the frequency responses of η_n, η and q-factor for these seven

https://doi.org/10.1017/jfm.2019.656 Published online by Cambridge University Press

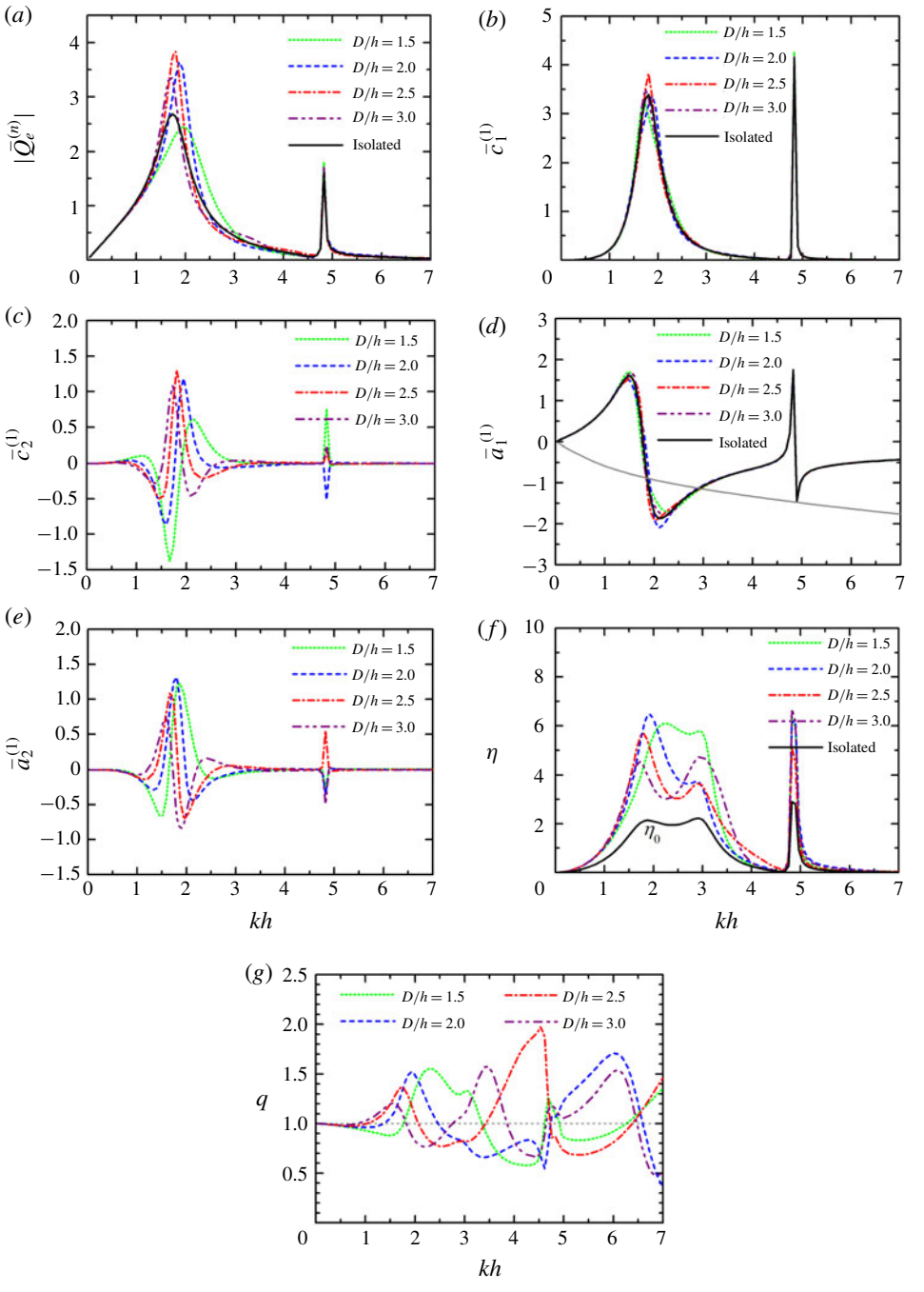


FIGURE 15. (Colour online) Comparison for different spacing distance between the OWCs, D/h, with $N = 2$, $R/h = 0.5$, $(R - R_i)/h = 0.1$, $d/h = 0.2$, $\beta = \pi/2$ and $h = 10$ m: (*a*) $|\bar{Q}_e^{(n)}|$; (*b*) $\bar{c}_1^{(1)}$; (*c*) $\bar{c}_2^{(1)}$; (*d*) $\bar{a}_1^{(1)}$ and $-\bar{a}_{PTO}$; (*e*) $\bar{a}_2^{(1)}$; (*f*) η; and (*g*) q-factor.

cases. Figure 17(*a*) demonstrates that, for $kh \in (2.1, 2.8)$, when the second and the fourth OWCs are placed closer to the ends of the array (i.e. $\Delta D/h > 0$), more power

https://doi.org/10.1017/jfm.2019.656 Published online by Cambridge University Press

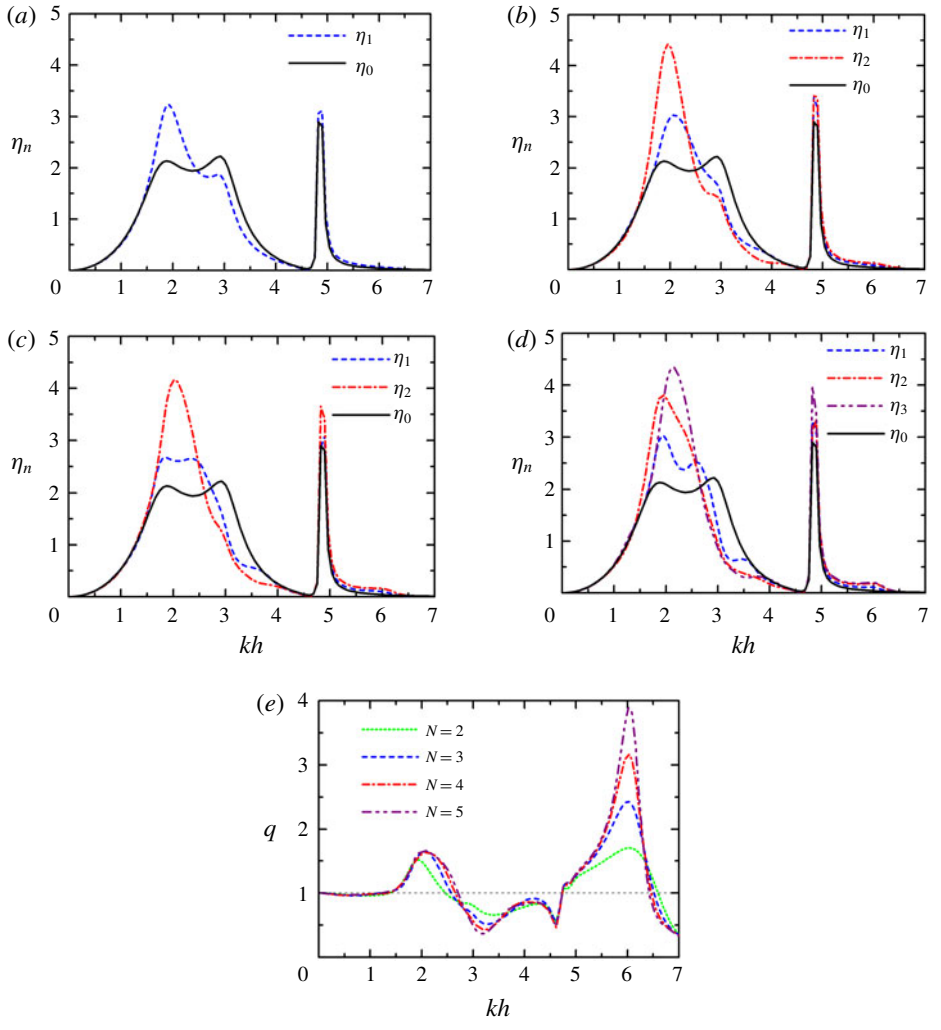


FIGURE 16. (Colour online) Comparison for different number of the OWCs, N, with $R/h = 0.5$, $(R - R_i)/h = 0.1$, $d/h = 0.2$, $D/h = 2.0$, $\beta = \pi/2$ and $h = 10$ m: (*a*) η_n with $N = 2$; (*b*) η_n with $N = 3$; (*c*) η_n with $N = 4$; (*d*) η_n with $N = 5$; and (*e*) q-factor.

can be captured by the two OWCs at the ends of the array compared to the uniform distribution (i.e. $\Delta D/h = 0$). Whereas when the second and the fourth OWCs are placed closer to the central OWC (i.e. $\Delta D/h < 0$), less power can be captured by the two end OWCs.

On the contrary, figure 17(*c*) indicates an opposite effect of $\Delta D/h$ on the power absorption of the central OWC in terms of the peak value of η_3: the peak value of η_3 is no more than 3.0 for $\Delta D/h > 0$, while it can be larger than 4.3 for each case with $\Delta D/h \leqslant 0$. As shown in figure 17(*b*), the shape of the η_2 curve is significantly influenced by $\Delta D/h$. As $|\Delta D/h|$ increases from 0 to 1.5, the η_2 curve at $kh \in (1.5, 3.5)$ turns from a single peak curve into a bimodal curve. The less uniform the array layout, i.e. the larger $|\Delta D/h|$, the greater the separation between the two peaks of the curve. This is reasonable, since the hydrodynamic interaction between each pair of adjacent OWCs is dependent on the distance between them (as demonstrated in

https://doi.org/10.1017/jfm.2019.656 Published online by Cambridge University Press

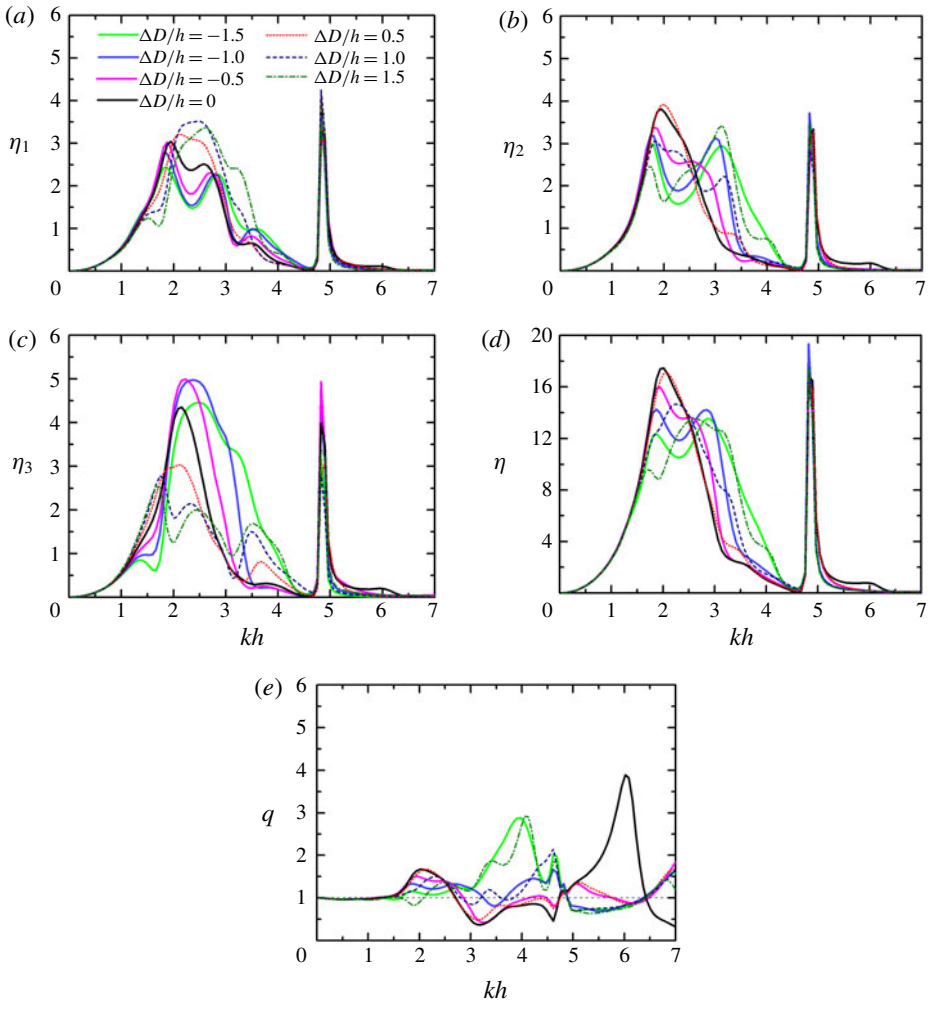


FIGURE 17. (Colour online) Comparison for different distance difference, $\Delta D/h$, with $N = 5$, $R/h = 0.5$, $(R - R_i)/h = 0.1$, $d/h = 0.2$, $D_1 + D_2 + D_3 + D_4 = 8h$, $D_1 = D_4$, $D_2 = D_3$, $\beta = \pi/2$ and $h = 10$ m: (*a*) η_1; (*b*) η_2; (*c*) η_3; (*d*) η; and (*e*) q-factor.

figure 15), leading to two reinforcing peaks of η_2 at two different frequencies when $|(D_2 - D_1)/h| = |\Delta D/h|$ is large enough. Figure 17(*d*) indicates that the main peak of the total wave power capture factor of the array, η, for $\Delta D/h = 0$ and 0.5, is larger than in other cases. Of these two options, the array with $\Delta D/h = 0.5$ might be of greater practical interest, for the power captured by each OWC is more balanced than in the case with $\Delta D/h = 0$.

Although the peak value of η is reduced with a non-uniform array layout, the peak is broadened. Therefore, the array with different distances may well be attractive in practice, especially for a broad-banded wave spectrum. A peak value of the q-factor larger than 2.9 is achieved for $\Delta D/h = \pm 1.5$ around $kh = 4.0$. Thanks to the constructive hydrodynamic interaction, the array with $\Delta D/h = \pm 1.5$ absorbs more power than the other cases for $kh \in (3.1, 4.3)$.

https://doi.org/10.1017/jfm.2019.656 Published online by Cambridge University Press

6. Conclusions

An array of coast-integrated OWCs is considered in this paper. The chamber of each OWC is mainly composed of a hollow vertical circular cylinder. Each OWC cylinder is half-embedded in the wall, with the other half on the seaward side open from a finite submergence to the seabed. Based on the linear potential flow theory and eigenfunction matching method, a theoretical model was developed to solve the wave scattering and wave radiation problems of these OWCs. The effects induced by the Wells turbine installed at the top of each OWC and the compressibility of air inside each chamber were represented by a linear PTO system. The present theoretical model was developed without the thin-wall restriction; hence the influence of the wall thickness of the OWC chamber on power extraction can be examined. The performances of the multiple and single coast-integrated/offshore OWCs in wave power extraction were compared with each other. The theoretical model was ultimately applied to explore the influence of the wave conditions, chamber size, spacing between the OWCs and number of OWCs on power extraction. The following conclusions may be drawn.

Wave reflection at the coast plays a constructive role in wave power absorption for most of the wave conditions examined. The hydrodynamic interaction between the coast-integrated OWCs, which is referred to in this work as the array effect, can enhance power extraction of the OWCs dramatically. A dramatic peak wave power capture factor, much higher than that of a single offshore/coast-integrated OWC and of multiple offshore OWCs, can be achieved due to both the constructive array effect and the constructive coast effect. For any certain wave frequency, there is a general identity, i.e. (5.1), of the optimum wave capture factor over all incidence angles that multiple coast-integrated OWCs must hold regardless of the OWC dimension. It means a higher peak in the curve of wave power capture factor at some incident wave directions must be associated with less power absorption at other wave incident angles.

As the radius of the coast-integrated OWC chambers increases, the main peaks of the frequency response curve of power capture factor shift towards lower wave frequencies and gain intensity. The wall thickness and submergence of the OWC chambers should be as small as possible to yield high wave power extraction across a broad bandwidth.

The spacing between two coast-integrated OWCs has a strong effect on the shape of the array factor frequency response curve as well as on its amplitude. For multiple coast-integrated OWCs with the same spacing, the one(s) closest to the central position has the highest peak power capture factor. The power absorption by individual OWCs in an array can be balanced and the frequency response of the overall wave capture factor can be improved by adopting a non-uniform array layout.

The linear approximation for small wave steepness was used throughout and no viscous effect was considered; hence the model is not suitable for extreme wave–structure interactions. In future work we will consider the optimization of the array from a general point of view, i.e. considering directional wave spectra, coast-integrated OWCs with different geometries (different diameters, wall thicknesses and submergences) and more elaborate PTO control strategies. ‘Near-trapping’ effects as described by, for example, Maniar & Newman (1997) and Thompson, Linton & Porter (2008) were not registered in our results. However, this is an aspect of interest that we plan to investigate as a continuation of this line of research.

https://doi.org/10.1017/jfm.2019.656 Published online by Cambridge University Press

Acknowledgements

The research was supported by Intelligent Community Energy (ICE), INTERREG V FCE, European Commission (contract no. 5025) and the National Natural Science Foundation of China (51679124, 51879144).

Appendix A. Integral equations of the scattering/radiation problems

Inserting (3.1) and (3.6) into (3.14), after multiplying both sides by $Z_\zeta(z)\mathrm{e}^{-\mathrm{i}\tau\theta_n}$ and integrating for $z\in[-h,0]$ and $\theta_n\in[0,2\pi]$, for any pair of integers (τ,ζ), it can be shown that

$$2\pi h A^{\chi,n}_{\tau,\zeta} = \sum_{l=0}^{\infty}\left[\frac{\pi}{\varepsilon_{|\tau|}}(X^{(1,n)}_{|\tau|,l}C^{\chi,n}_{|\tau|,l}+Y^{(1,n)}_{|\tau|,l}D^{\chi,n}_{|\tau|,l}) + \mathrm{i}\sum_{\substack{m=0,\\ m\neq|\tau|}}^{\infty}\frac{\tau[(-1)^{\tau-m}-1]}{\tau^2-m^2}(X^{(1,n)}_{m,l}C^{\chi,n}_{m,l}+Y^{(1,n)}_{m,l}D^{\chi,n}_{m,l})\right]L^{(n)}_{l,\zeta}, \tag{A 1}$$

in which

$$X^{(1,n)}_{m,l}=\begin{cases}\dfrac{m}{R_n}\left(\dfrac{R_{i,n}}{R_n}\right)^{m-1}, & l=0,\\ \dfrac{\beta_{n,l}\mathrm{I}'_m(\beta_{n,l}R_{i,n})}{\mathrm{I}_m(\beta_{n,l}R_n)}, & l\neq0,\end{cases}\qquad Y^{(1,n)}_{m,l}=\begin{cases}\dfrac{1}{R_{i,n}}, & l=0,\ m=0,\\ -\dfrac{m}{R_n}\left(\dfrac{R_n}{R_{i,n}}\right)^{m+1}, & l=0,\ m\neq0,\\ \dfrac{\beta_{n,l}\mathrm{K}'_m(\beta_{n,l}R_{i,n})}{\mathrm{K}_m(\beta_{n,l}R_n)}, & l\neq0,\end{cases} \tag{A 2a,b}$$

$$L^{(n)}_{l,\zeta} = \int_{-h}^{-d_n}\cos[\beta_{n,l}(z+h)]Z_\zeta(z)\,\mathrm{d}z = \begin{cases}\dfrac{(-1)^l(h-d_n)^2k_0Z_0(0)\sinh[k_0(h-d_n)]}{[(h-d_n)^2k_0^2+l^2\pi^2]\cosh(k_0h)}, & \zeta=0,\\ \dfrac{(-1)^l(h-d_n)^2k_\zeta Z_\zeta(0)\sin[k_\zeta(h-d_n)]}{[(h-d_n)^2k_\zeta^2-l^2\pi^2]\cos(k_\zeta h)}, & \zeta\neq0.\end{cases} \tag{A 3}$$

Inserting (3.6) and (3.13) into (3.15), after multiplying both sides by $Z_\zeta(z)\cos(\tau\theta_n)$ and integrating for $z\in[-h,0]$ and $\theta_n\in[0,\pi]$, for any pair of integers (τ,ζ), it can be shown that

$$\sum_{l=0}^{\infty}(X^{(2,n)}_{\tau,l}C^{\chi,n}_{\tau,l}+Y^{(2,n)}_{\tau,l}D^{\chi,n}_{\tau,l})L^{(n)}_{l,\zeta}-hZ^{(2,n)}_{\tau,\zeta}E^{\chi,n}_{\tau,\zeta}-\sum_{\substack{j=1,\\ j\neq n}}^{N}\sum_{m=0}^{\infty}E^{\chi,j}_{m,\zeta}T'^{n,j}_{m,\tau,\zeta} = -\frac{2\delta_{\chi,0}\delta_{\zeta,0}\varepsilon_\tau\mathrm{i}gAk_0h}{\omega Z_0(0)}\mathrm{e}^{-\mathrm{i}k_0x_n\cos\beta}(-\mathrm{i})^\tau\mathrm{J}'_\tau(k_0R_n)\cos(\tau\beta), \tag{A 4}$$

where

$$T'^{n,j}_{m,\tau,\zeta}=\frac{\varepsilon_\tau k_\zeta h\tilde{\mathrm{I}}'_\tau(k_\zeta R_n)}{2\tilde{\mathrm{K}}_m(k_\zeta R_j)}[\tilde{\mathrm{K}}_{m+\tau}(k_\zeta R_{jn})+(-1)^{\tau\delta_{\zeta,0}}\tilde{\mathrm{K}}_{m-\tau}(k_\zeta R_{jn})]\mathrm{e}^{\mathrm{i}(m\alpha_{jn}+\tau\alpha_{nj})}, \tag{A 5}$$

https://doi.org/10.1017/jfm.2019.656 Published online by Cambridge University Press

$$X^{(2,n)}_{\tau,\zeta}=\begin{cases}\dfrac{\tau}{R_n}, & \zeta=0,\\ \dfrac{\beta_{n,\zeta}\mathrm{I}'_\tau(\beta_{n,\zeta}R_n)}{\mathrm{I}_\tau(\beta_{n,\zeta}R_n)}, & \zeta\neq 0,\end{cases}\qquad Y^{(2,n)}_{\tau,\zeta}=\begin{cases}\dfrac{1}{R_n}, & \zeta=0,\ \tau=0,\\ -\dfrac{\tau}{R_n}, & \zeta=0,\ \tau\neq 0,\\ \dfrac{\beta_{n,\zeta}\mathrm{K}'_\tau(\beta_{n,\zeta}R_n)}{\mathrm{K}_\tau(\beta_{n,\zeta}R_n)}, & \zeta\neq 0,\end{cases}\tag{A 6a,b}$$

$$Z^{(2,n)}_{\tau,\zeta}=\begin{cases}\dfrac{k_0\mathrm{H}'_\tau(k_0R_n)}{\mathrm{H}_\tau(k_0R_n)}, & \zeta=0,\\ \dfrac{k_\zeta\mathrm{K}'_\tau(k_\zeta R_n)}{\mathrm{K}_\tau(k_\zeta R_n)}, & \zeta=1,2,3,\ldots.\end{cases}\tag{A 7}$$

Inserting (3.1) and (3.6) into (3.16), after multiplying both sides by $\cos[\beta_{n,\zeta}(z+h)]\cos(\tau\theta_n)$ and integrating for $z\in[-h,-d_n]$ and $\theta_n\in[0,\pi]$, for any pair of integers (τ,ζ), it can be shown that

$$\begin{aligned}&\sum_{l=0}^{\infty}\left[\frac{\pi}{2}\left(\frac{\tilde{\mathrm{I}}_\tau(k_lR_{i,n})}{k_l\tilde{\mathrm{I}}'_\tau(k_lR_{i,n})}A^{\chi,n}_{\tau,l}+\frac{\tilde{\mathrm{I}}_{-\tau}(k_lR_{i,n})}{k_l\tilde{\mathrm{I}}'_{-\tau}(k_lR_{i,n})}A^{\chi,n}_{-\tau,l}\right)\right.\\ &\qquad\left.-\mathrm{i}\sum_{\substack{m=-\infty,\\ m\neq\pm\tau}}^{\infty}\frac{m[(-1)^{m-\tau}-1]}{m^2-\tau^2}\frac{\tilde{\mathrm{I}}_m(k_lR_{i,n})}{k_l\tilde{\mathrm{I}}'_m(k_lR_{i,n})}A^{\chi,n}_{m,l}\right]L^{(n)}_{\zeta,l}\\ &\quad=\frac{\pi(h-d_n)}{\varepsilon_\tau\varepsilon_\zeta}(X^{(3,n)}_{\tau,\zeta}C^{\chi,n}_{\tau,\zeta}+Y^{(3,n)}_{\tau,\zeta}D^{\chi,n}_{\tau,\zeta})+\frac{\delta_{\chi,n}\delta_{\tau,0}\delta_{\zeta,0}\mathrm{i}\pi(h-d_n)}{\rho\omega},\end{aligned}\tag{A 8}$$

where

$$X^{(3,n)}_{\tau,\zeta}=\begin{cases}\left(\dfrac{R_{i,n}}{R_n}\right)^\tau, & \zeta=0,\\ \dfrac{\mathrm{I}_\tau(\beta_{n,\zeta}R_{i,n})}{\mathrm{I}_\tau(\beta_{n,\zeta}R_n)}, & \zeta\neq 0,\end{cases}\qquad Y^{(3,n)}_{\tau,\zeta}=\begin{cases}1+\ln\left(\dfrac{R_{i,n}}{R_n}\right), & \zeta=0,\ \tau=0,\\ \left(\dfrac{R_n}{R_{i,n}}\right)^\tau, & \zeta=0,\ \tau\neq 0,\\ \dfrac{\mathrm{K}_\tau(\beta_{n,\zeta}R_{i,n})}{\mathrm{K}_\tau(\beta_{n,\zeta}R_n)}, & \zeta\neq 0.\end{cases}\tag{A 9a,b}$$

Inserting (3.6) and (3.13) into (3.17), after multiplying both sides by $\cos[\beta_n,\zeta(z+h)]\cos(\tau\zeta_n)$ and integrating for $z\in[-h,-d_n]$ and $\theta_n\in[0,\pi]$, for any pair of integers (τ,ζ), the following expression is obtained

$$\begin{aligned}&\frac{h-d_n}{\varepsilon_\zeta}(C^{\chi,n}_{\tau,\zeta}+D^{\chi,n}_{\tau,\zeta})-\sum_{l=0}^{\infty}E^{\chi,n}_{\tau,l}L^{(n)}_{\zeta,l}-\sum_{\substack{j=1,\\ j\neq n}}^{N}\sum_{m=0}^{\infty}\sum_{l=0}^{\infty}E^{\chi,j}_{m,l}T^{n,j}_{m,\tau,l}L^{(n)}_{\zeta,l}\\ &\quad=-\frac{2\delta_{\chi,0}\varepsilon_\tau\mathrm{i}gAL^{(n)}_{\zeta,0}}{\omega Z_0(0)}\mathrm{e}^{-\mathrm{i}k_0x_n\cos\beta}(-\mathrm{i})^\tau\mathrm{J}_\tau(k_0R_n)\cos(\tau\beta),\end{aligned}\tag{A 10}$$

in which

$$T^{n,j}_{m,\tau,l}=\frac{\varepsilon_\tau\tilde{\mathrm{I}}_\tau(k_lR_n)}{2\tilde{\mathrm{K}}_m(k_lR_j)}[\tilde{\mathrm{K}}_{m+\tau}(k_lR_{jn})+(-1)^{\tau\delta_{l,0}}\tilde{\mathrm{K}}_{m-\tau}(k_lR_{jn})]\mathrm{e}^{\mathrm{i}(m\alpha_{jn}+\tau\alpha_{nj})}.\tag{A 11}$$

https://doi.org/10.1017/jfm.2019.656 Published online by Cambridge University Press

A linear algebraic system can be formed by (A 1), (A 4), (A 8) and (A 10), and can be used to solve the unknown coefficients $A_{m,l}^{\chi,n}$, $C_{m,l}^{\chi,n}$, $D_{m,l}^{\chi,n}$ and $E_{m,l}^{\chi,n}$ numerically after truncation. In the present model, the infinite terms of $\mathrm{e}^{-\mathrm{i}m\theta_n}/\cos(m\theta_n)$ and $Z_l(z)/\cos[\beta_{n,l}(z+h)]$ are truncated at $m=M$ and $l=L$, respectively. Accurate results can be obtained by choosing $M=12$ and $L=20$.

Appendix B. Identity of optimum wave capture factor over all incidence angles

Following Evans (1980) and Falnes (1980), the theoretical maximum power that may be extracted by multiple coast-integrated OWCs can be expressed as

$$P_{MAX}=\tfrac{1}{8}\boldsymbol{Q}_e^{\dagger}(\beta)\boldsymbol{C}^{-1}\boldsymbol{Q}_e(\beta), \tag{B 1}$$

which is obtained when an ideal PTO system is applied, such that

$$\boldsymbol{p}(\beta)=\boldsymbol{p}_{opt}(\beta)=\tfrac{1}{2}\boldsymbol{C}^{-1}\boldsymbol{Q}_e(\beta) \tag{B 2}$$

is satisfied (provided $\boldsymbol{C}$ is non-singular).

Note that $\boldsymbol{C}$ is composed of real elements, and, more specifically, it can be shown from (3.20) that $\boldsymbol{C}$ is symmetric. Assuming $\boldsymbol{C}$ is positive definite (Wolgamot *et al.* 2012), $\boldsymbol{C}$ can be written as the product of an upper real triangular matrix $\boldsymbol{H}$ and its transpose with the employment of the Cholesky decomposition,

$$\boldsymbol{C}=\boldsymbol{H}^{\mathrm{T}}\boldsymbol{H}, \tag{B 3}$$

where T denotes the conjugate transpose. Hence,

$$\boldsymbol{C}^{-1}=\boldsymbol{H}^{-1}(\boldsymbol{H}^{\mathrm{T}})^{-1}. \tag{B 4}$$

For the sake of convenience, a column vector of length N is defined as (Wolgamot *et al.* 2012)

$$\boldsymbol{S}(\beta)=(\boldsymbol{H}^{\mathrm{T}})^{-1}\boldsymbol{Q}_e(\beta), \tag{B 5}$$

from which (B 1) can be rewritten as

$$P_{MAX}(\beta)=\tfrac{1}{8}\boldsymbol{S}^{\dagger}(\beta)\boldsymbol{S}(\beta). \tag{B 6}$$

Rewriting (3.20) in the matrix format gives

$$\boldsymbol{C}=\frac{k}{8\pi\rho g c_g A^2}\int_0^{\pi}\boldsymbol{Q}_e(\beta)\boldsymbol{Q}_e^{\dagger}(\beta)\,\mathrm{d}\beta. \tag{B 7}$$

Multiplying two $\boldsymbol{H}$ related inverse matrices results in

$$(\boldsymbol{H}^{\mathrm{T}})^{-1}\boldsymbol{C}\boldsymbol{H}^{-1}=\frac{k}{8\pi\rho g c_g A^2}\int_0^{\pi}\boldsymbol{S}(\beta)\boldsymbol{S}^{\dagger}(\beta)\,\mathrm{d}\beta=\boldsymbol{I}, \tag{B 8}$$

leading to the integral

$$\int_0^{\pi}S_i(\beta)S_j^{*}(\beta)\,\mathrm{d}\beta=\delta_{i,j}\frac{8\pi\rho g c_g A^2}{k}. \tag{B 9}$$

https://doi.org/10.1017/jfm.2019.656 Published online by Cambridge University Press

Integrating (B 6) over $\beta \in [0, \pi]$ and adopting (B 9) gives

$$\int_0^{\pi} P_{MAX}\,\mathrm{d}\beta = \frac{N\pi\rho g c_g A^2}{k} \tag{B 10}$$

and

$$\frac{1}{\pi}\int_0^{\pi} \eta_{MAX}(\beta)\,\mathrm{d}\beta = \frac{2k}{\pi\rho g c_g A^2}\int_0^{\pi} P_{MAX}(\beta)\,\mathrm{d}\beta = 2N. \tag{B 11}$$

REFERENCES

Abramowitz, M. & Stegun, I. A. 1964 *Handbook of Mathematical Functions*. Government Printing Office.

Arena, F., Romolo, A., Malara, G., Fiamma, V. & Laface, V. 2017 The first full operative U-OWC plants in the port of civitavecchia. In *ASME 2017 36th International Conference on Ocean, Offshore and Arctic Engineering*, American Society of Mechanical Engineers, p. V010T09A022.

Astariz, S. & Iglesias, G. 2015 The economics of wave energy: a review. *Renew. Sustainable Energy Rev.* **45**, 397–408.

Boccotti, P. 2007 Caisson breakwaters embodying an OWC with a small opening-part I: theory. *Ocean Engng* **34** (5–6), 806–819.

Clément, A., McCullen, P., Falcão, A. F., de, O., Fiorentino, A., Gardner, F., Hammarlund, K., Lemonis, G., Lewis, T., Nielsen, K. *et al.* 2002 Wave energy in Europe: current status and perspectives. *Renew. Sustainable Energy Rev.* **6** (5), 405–431.

Di Lauro, E., Lara, J. L., Maza, M., Losada, I. J., Contestabile, P. & Vicinanza, D. 2019 Stability analysis of a non-conventional breakwater for wave energy conversion. *Coast. Engng* **145**, 36–52.

Drew, B., Plummer, A. R. & Sahinkaya, M. N. 2009 A review of wave energy converter technology. *Proc. Inst. Mech. Engrs* A **223** (A8), 887–902.

Elhanafi, A., Fleming, A., Macfarlane, G. & Leong, Z. 2016 Numerical energy balance analysis for an onshore oscillating water column–wave energy converter. *Energy* **116**, 539–557.

Elhanafi, A., Fleming, A., Macfarlane, G. & Leong, Z. 2017 Underwater geometrical impact on the hydrodynamic performance of an offshore oscillating water column–wave energy converter. *Renew. Energy* **105**, 209–231.

Evans, D. V. 1980 *Some Analytic Results for Two- and Three-Dimensional Wave-Energy Absorbers*. Academic Press.

Evans, D. V. 1988 The maximum efficiency of wave-energy devices near coast lines. *Appl. Ocean Res.* **10** (3), 162–164.

Evans, D. V. & Porter, R. 1995 Hydrodynamic characteristics of an oscillating water column device. *Appl. Ocean Res.* **17** (3), 155–164.

Falcão, A. F. de O. & Henriques, J. C. C 2016 Oscillating-water-column wave energy converters and air turbines: a review. *Renew. Energy* **85**, 1391–1424.

Falcão, A. F. de O., Henriques, J. C. C. & Gato, L. M. C. 2016 Air turbine optimization for a bottom-standing oscillating-water-column wave energy converter. *J. Ocean Engng Marine Energy* **2** (4), 459–472.

Falnes, J. 1980 Radiation impedance matrix and optimum power absorption for interacting oscillators in surface waves. *Appl. Ocean Res.* **2** (2), 75–80.

Falnes, J. 2002 *Ocean Waves and Oscillating Systems: Linear Interactions Including Wave-energy Extraction*. Cambridge University Press.

He, F., Huang, Z. & Law, A. W. K. 2012 Hydrodynamic performance of a rectangular floating breakwater with and without pneumatic chambers: an experimental study. *Ocean Engng* **51**, 16–27.

https://doi.org/10.1017/jfm.2019.656 Published online by Cambridge University Press

HE, F., LENG, J. & ZHAO, X. 2017 An experimental investigation into the wave power extraction of a floating box-type breakwater with dual pneumatic chambers. *Appl. Ocean Res.* **67**, 21–30.

HE, F., ZHANG, H., ZHAO, J., ZHENG, S. & IGLESIAS, G. 2019 Hydrodynamic performance of a pile-supported OWC breakwater: an analytical study. *Appl. Ocean Res.* **88**, 326–340.

HEATH, T. V. 2012 A review of oscillating water columns. *Phil. Trans. R. Soc. Lond.* A **370** (1959), 235–245.

HENRIQUES, J. C. C., GATO, L. M. C., FALCÃO, A. F., DE, O., ROBLES, E. & FAŸ, F. X 2016 Latching control of a floating oscillating-water-column wave energy converter. *Renew. Energy* **90**, 229–241.

HERAS-SAIZARBITORIA, I., ZAMANILLO, I. & LASKURAIN, I. 2013 Social acceptance of ocean wave energy: a case study of an OWC shoreline plant. *Renew. Sustainable Energy Rev.* **27**, 515–524.

HOWE, D. & NADER, J. R. 2017 OWC WEC integrated within a breakwater versus isolated: experimental and numerical theoretical study. *Intl J. Marine Energy* **20**, 165–182.

KONISPOLIATIS, D. N. & MAVRAKOS, S. A. 2016 Hydrodynamic analysis of an array of interacting free-floating oscillating water column (OWC's) devices. *Ocean Engng* **111**, 179–197.

KURNIAWAN, A., CHAPLIN, J. R., GREAVES, D. M. & HANN, M. 2017 Wave energy absorption by a floating air bag. *J. Fluid Mech.* **812**, 294–320.

LÓPEZ, I., CARBALLO, R., TAVEIRA-PINTO, F. & IGLESIAS, G. 2020 Sensitivity of OWC performance to air compressibility. *Renew. Energy* **145**, 1334–1347.

LÓPEZ, I. & IGLESIAS, G. 2014 Efficiency of OWC wave energy converters: a virtual laboratory. *Appl. Ocean Res.* **44**, 63–70.

LÓPEZ, I., PEREIRAS, B., CASTRO, F. & IGLESIAS, G. 2014 Optimisation of turbine-induced damping for an OWC wave energy converter using a RANS–VOF numerical model. *Appl. Energy* **127**, 105–114.

LÓPEZ, I., PEREIRAS, B., CASTRO, F. & IGLESIAS, G. 2016 Holistic performance analysis and turbine-induced damping for an OWC wave energy converter. *Renew. Energy* **85**, 1155–1163.

LOVAS, S., MEI, C. C. & LIU, Y. 2010 Oscillating water column at a coastal corner for wave power extraction. *Appl. Ocean Res.* **32** (3), 267–283.

MANIAR, H. D. & NEWMAN, J. N. 1997 Wave diffraction by a long array of cylinders. *J. Fluid Mech.* **339**, 309–330.

MARTINS-RIVAS, H. & MEI, C. C. 2009*a* Wave power extraction from an oscillating water column along a straight coast. *Ocean Engng* **36** (6–7), 426–433.

MARTINS-RIVAS, H. & MEI, C. C. 2009*b* Wave power extraction from an oscillating water column at the tip of a breakwater. *J. Fluid Mech.* **626**, 395–414.

MICHELE, S., SAMMARCO, P. & D'ERRICO, M. 2016 The optimal design of a flap gate array in front of a straight vertical wall: resonance of the natural modes and enhancement of the exciting torque. *Ocean Engng* **118**, 152–164.

MORRIS-THOMAS, M. T., IRVIN, R. J. & THIAGARAJAN, K. P. 2007 An investigation into the hydrodynamic efficiency of an oscillating water column. *J. Offshore Mech. Arctic Engng* **129** (4), 273–278.

MUSTAPA, M. A., YAAKOB, O. B., AHMED, Y. M., RHEEM, C. K., KOH, K. K. & ADNAN, F. A. 2017 Wave energy device and breakwater integration: a review. *Renew. Sustainable Energy Rev.* **77**, 43–58.

NADER, J. R., ZHU, S. P. & COOPER, P. 2014 Hydrodynamic and energetic properties of a finite array of fixed oscillating water column wave energy converters. *Ocean Engng* **88**, 131–148.

NADER, J. R., ZHU, S. P., COOPER, P. & STAPPENBELT, B. 2012 A finite-element study of the efficiency of arrays of oscillating water column wave energy converters. *Ocean Engng* **43**, 72–81.

NIHOUS, G. C. 2012 Wave power extraction by arbitrary arrays of non-diffracting oscillating water columns. *Ocean Engng* **51**, 94–105.

NING, D., ZHOU, Y. & ZHANG, C. 2018 Hydrodynamic modeling of a novel dual-chamber OWC wave energy converter. *Appl. Ocean Res.* **78**, 180–191.

https://doi.org/10.1017/jfm.2019.656 Published online by Cambridge University Press

PAWITAN, K. A., DIMAKOPOULOS, A. S., VICINANZA, D., ALLSOP, W. & BRUCE, T. 2019 A loading model for an OWC caisson based upon large-scale measurements. *Coast. Engng* **145**, 1–20.

PEREIRAS, B., LÓPEZ, I., CASTRO, F. & IGLESIAS, G. 2015 Non-dimensional analysis for matching an impulse turbine to an OWC (oscillating water column) with an optimum energy transfer. *Energy* **87**, 481–489.

RUSU, E. & ONEA, F. 2018 A review of the technologies for wave energy extraction. *Clean Energy* **2** (1), 10–19.

SARKAR, D., RENZI, E. & DIAS, F. 2015 Effect of a straight coast on the hydrodynamics and performance of the Oscillating Wave Surge Converter. *Ocean Engng* **105**, 25–32.

SARMENTO, A. J. N. A. & FALCÃO, A. F. DE O. 1985 Wave generation by an oscillating surface-pressure and its application in wave-energy extraction. *J. Fluid Mech.* **150**, 467–485.

SHENG, W. & LEWIS, A. 2018 Power takeoff optimization to maximize wave energy conversions for oscillating water column devices. *IEEE J. Ocean. Engng* **43** (1), 36–47.

THOMPSON, I., LINTON, C. M. & PORTER, R. 2008 A new approximation method for scattering by long finite arrays. *Q. J. Mech. Appl. Maths* **61** (3), 333–352.

VIVIANO, A., NATY, S., FOTI, E., BRUCE, T., ALLSOP, W. & VICINANZA, D. 2016 Large-scale experiments on the behaviour of a generalised oscillating water column under random waves. *Renew. Energy* **99**, 875–887.

WOLGAMOT, H. A., TAYLOR, P. H. & TAYLOR, R. E. 2012 The interaction factor and directionality in wave energy arrays. *Ocean Engng* **47**, 65–73.

YU, H., ZHENG, S., ZHANG, Y. & IGLESIAS, G. 2019 Wave radiation from a truncated cylinder of arbitrary cross section. *Ocean Engng* **173**, 519–530.

ZHANG, C. & NING, D. 2019 Hydrodynamic study of a novel breakwater with parabolic openings for wave energy harvest. *Ocean Engng* **182**, 540–551.

ZHANG, Y., ZOU, Q. P. & GREAVES, D. 2012 Airwater two-phase flow modelling of hydrodynamic performance of an oscillating water column device. *Renew. Energy* **41**, 159–170.

ZHAO, X., NING, D., JOHANNING, L. & TENG, B. 2018 Numerical investigation on hydrodynamic performance of a wec array integrated into a pontoon. In *The 28th International Ocean and Polar Engineering Conference*, International Society of Offshore and Polar Engineers.

ZHENG, S. & ZHANG, Y. 2015 Wave diffraction from a truncated cylinder in front of a vertical wall. *Ocean Engng* **104**, 329–343.

ZHENG, S. & ZHANG, Y. 2016 Wave radiation from a truncated cylinder in front of a vertical wall. *Ocean Engng* **111**, 602–614.

ZHENG, S. & ZHANG, Y. 2018 Theoretical modelling of a new hybrid wave energy converter in regular waves. *Renew. Energy* **128**, 125–141.

ZHENG, S., ZHANG, Y. & IGLESIAS, G. 2018 Wave–structure interaction in hybrid wave farms. *J. Fluids Struct.* **83**, 386–412.

ZHENG, S., ZHANG, Y. & IGLESIAS, G. 2019 Coast/breakwater-integrated OWC: a theoretical model. *Mar. Struct.* **66**, 121–135.

https://doi.org/10.1017/jfm.2019.656 Published online by Cambridge University Press